Reactive transport modeling of geologic CO_2 sequestration in saline aquifers: the influence of intra-aquifer shales and the relative effectiveness of structural, solubility, and mineral trapping during prograde and retrograde sequestration

James W. Johnson (jwjohnson@llnl.gov),
John J. Nitao (nitao@llnl.gov),
Carl I. Steefel (steefel@llnl.gov),
Kevin G. Knauss (knauss@llnl.gov)

Lawrence Livermore National Laboratory
Geosciences and Environmental Technologies Division
L-219, P.O. Box 808
Livermore, CA 94550

Introduction

One of the industrial revolution's most insidious environmental legacies—dangerous atmospheric concentrations of CO_2—can no longer be ignored. With "business-as-usual" projections rapidly approaching a grim horizon of climatic consequences, there is an urgent need to develop innovative strategies for CO_2 stabilization that either reduce emissions through improved energy efficiency, or eliminate them through waste-stream capture and sequestration. The latter approach currently stands alone as a potential near-term means of significantly curbing atmospheric CO_2 emissions.

Among proposed sequestration strategies, injection into confined geologic formations—in particular, saline aquifers—represents one of the most promising alternatives. Scientific viability of this approach hinges on the relative effectiveness of CO_2 migration and sequestration processes in the subsurface, while its successful implementation relies on our ability to predict sensitivity of this migration/sequestration balance to key physical and chemical characteristics of potential target reservoirs. Quantitative predictions of this kind can be used to establish those geochemical, hydrologic, and structural constraints that swing the balance most strongly in our—sequestration's—favor. Correlation of these constraints with the relevant properties of potential target formations can then identify those sites most likely to achieve optimal sequestration performance in terms of both isolation security and storage capacity.

Quantifying the relationship between CO_2 migration/sequestration balance and key formation characteristics requires a computational capability that explicitly couples multiphase-flow processes and kinetically-controlled geochemical processes. This capability must also interface smoothly with comprehensive thermodynamic/kinetic databases and versatile graphics utilities on the pre- and post-processing ends. We have developed a unique software package that meets these criteria; it integrates a state-of-the-art reactive transport simulator (NUFT [Nitao, 1998a]),

comprehensive supporting geochemical software and thermodynamic/kinetic databases (SUPCRT92 [Johnson et al., 1992; Shock, 1998], GEMBOCHS [Johnson and Lundeen, 1994a,b]), and a dedicated graphics utility (Xtool [Daveler, 1998]).

Our initial modeling work has focused on simulating CO_2 injection at Statoil's North-Sea Sleipner facility, where properties of the waste stream, target saline aquifer, and shale cap rock are relatively well constrained. The principle goal has been to discover and analyze the coupled-process mechanisms that lead to structural, solubility, and mineral trapping, and to quantify the relative effectiveness of these distinct sequestration processes as a function of key reservoir properties. Hence, although the simulations presented here are based on data available for the Sleipner site, the conclusions drawn from their analysis are equally relevant to the general saline-aquifer environment.

Objective

In this study, we address a series of fundamental questions regarding the processes and effectiveness of geologic CO_2 sequestration in saline aquifers.

We begin with the broadest: what is the ultimate fate of CO_2 injected into these environments? Once injected, it is immediately subject to two sets of competing processes: migration processes and sequestration processes. In terms of migration, the CO_2 moves by volumetric displacement of formation waters, with which it is largely immiscible; by gravity segregation, which causes the immiscible CO_2 plume to rise owing to its relatively low density; and by viscous fingering, owing to its relatively low viscosity. In terms of sequestration, some fraction of the rising plume will dissolve into formation waters (solubility trapping); some fraction may react with formation minerals to precipitate carbonates (mineral trapping); and the remaining portion eventually reaches the cap rock, where it migrates up-dip, potentially accumulating in local topographic highs (structural trapping).

Although this concept of competing migration/sequestration processes is intuitively obvious, identifying those sub-processes that dominate the competition is by no means straightforward. Hence, at present there are large uncertainties associated with the ultimate fate of injected CO_2 (Figure 1). Principal among these: can a typical shale cap rock provide a secure seal? Because gravity segregation will always keep the immiscible CO_2 plume moving towards the surface, cap-rock integrity is the single most important variable influencing isolation security. An extremely thick shale cap rock exists at Sleipner (several 100 m); here, however, we examine the performance of a 25-m-thick cap, which is more representative of the general case.

Although the cap rock represents the final barrier to vertical CO_2 migration, what is the effect of *intra*-aquifer permeability structure? Because this structure directs the path of all CO_2 migration processes within the target formation, it will effectively determine the spatial extent of plume-aquifer interaction, and thereby exert a controlling influence on all sequestration processes.

Here, we consider three common settings: a homogeneous saline aquifer, one with inter-bedded laterally continuous shales (continuum representation of microfractured shales), and one with inter-bedded laterally discontinuous shales (discrete representation of lateral facies changes). For each configuration, we examine the unique character of immiscible CO_2 migration paths, describe the dependent location, timing, and extent of associated solubility and mineral trapping, and detail the relative partitioning of injected CO_2 among the immiscible plume, formation waters, and carbonate precipitates.

While intra-aquifer permeability structure establishes the spatial framework of plume-aquifer interaction, the effectiveness of solubility and mineral trapping within this setting is largely determined by compositional characteristics of the aquifer and (if present) its inter-bedded shales. Here, we focus on Sleipner, where the saline aquifer consists of unconsolidated impure quartz sand saturated with a seawater-like aqueous phase, and there is strong evidence of thin inter-bedded shales. Based on our modeling results for this environment, we infer the effect of varying fluid composition from dilute to saline to brine, and the effect of varying sand and shale mineralogy within relevant limits. In addition, we describe those compositional characteristics required to maximize solubility and mineral trapping for a given permeability configuration.

We also address the fundamental yet infrequently posed question: what happens when CO_2 injection is terminated? Hydrologic and geochemical evolution may be very different during the relatively brief "prograde" (active-injection) and subsequent long-term "retrograde" (post-injection) regimes of geologic sequestration. Most importantly, are prograde trapping mechanisms enhanced or reversed during the retrograde phase (which spans geologic time scales)? We will demonstrate that there are indeed significant differences between prograde and retrograde sequestration.

Approach

To address the issues outlined above, we have carried out and analyzed three distinct Sleipner simulations using our integrated toolbox: NUFT, GEMBOCHS, and Xtool. In this section, we briefly review the relevant capabilities of these three software packages, present the adopted site-specific 2-D spatial domain and hydrologic/compositional data, and describe the thermodynamic/kinetic data used to represent chemical evolution within this system.

NUFT

NUFT (Nitao, 1998a), an integrated software package containing five application-specific program modules, facilitates numerical simulation of multiphase/multicomponent flow and reactive transport within a wide range of subsurface environments. This study requires use of modules USNT (Nitao, 1998b) and TRANS (Nitao, 2001), which implement an integrated finite-difference, spatial discretization to solve the flow and reactive-transport equations, using the Newton-Raphson method to solve the resulting nonlinear systems at each time step. The integrated model takes explicit account of multiphase advection, diffusion, dispersion, relative

permeability (extended Van Genuchten formulation [Parker et al., 1987]), and kinetically-controlled fluid-mineral reactions (rate law from transition state theory [Lasaga, 1998]). Moreover, it takes explicit account of *coupling between* these transport and geochemical processes through the dependence of permeability on porosity changes due to mineral precipitation/dissolution (normalized Kozeny equation [Scheidegger, 1974]), and through the dependence of fluid-phase volumetric saturation on immiscible CO_2 consumed or generated by fluid-mineral reactions.

At present, chemical interaction between and within distinct fluid phases (here, CO_2 and an aqueous phase) is governed by inter- and intra-phase equilibrium constraints. Activity coefficients for charged aqueous solutes are represented using an extended form of the Debye-Huckel equation (B-dot formulation: Helgeson, 1969), those for non-polar neutral solutes are represented using the Drummond (1981) model, and those for polar neutral solutes are taken to be unity.

The equation-of-state and viscosity formulations implemented for supercritical CO_2 are those developed by Span and Wagner (1996) and Fenghour (1998), respectively. The corresponding formulations implemented for H_2O are those presented by Meyer et al. (1993). Although PVT properties of the aqueous phase are here taken to be those of pure H_2O instead of a seawater-like saline fluid, this approximation introduces a negligible density difference (less than 0.3%) for the relevant P-T conditions (Fofonoff and Millard, 1983).

The aqueous phase is taken to be the wetting fluid; hence, chemical interaction of the immiscible CO_2 fluid and kinetically-reacting mineral grains occurs exclusively through a grain-surrounding aqueous-phase film, whose thickness can be conceptualized as inversely proportional to CO_2 volumetric saturation. The *residual* volumetric saturation of CO_2—the limit below which it is no longer a contiguous (advectively mobile) phase—is taken to be 0.05, which falls toward the low end of typical values. An immobile inert gas phase (volumetric saturation of 0.01) provides a pressure buffer for the initial evolution of immiscible CO_2 within grid cells due to geochemical reactions. Although necessary to achieve sufficiently large time stepping, this inert gas has no other influence on the simulations.

GEMBOCHS

The GEMBOCHS system integrates a comprehensive relational thermodynamic/kinetic database (GEMBOCHS) and dedicated software library (Jewel [Johnson and Lundeen,1994a], Facet [Johnson and Lundeen, 1995]) that together facilitate generation of application-specific thermodynamic/kinetic datafiles (e.g., Johnson and Lundeen, 1994b) for use with geochemical modeling codes (e.g., EQ3/6 [Wolery, 1992], GWB [Bethke, 1994]) and reactive transport software (e.g., NUFT [Nitao, 1998a], CRUNCH [Steefel, 2001]). The datafiles can be customized in terms of bulk composition, P-T conditions, and literature sources for both thermodynamic/kinetic data (reference-state properties, equation-of-state parameters, heat-capacity coefficients, and phase-transition data) and the equations of state and other algorithms used to extrapolate reference-state properties to elevated P-T conditions.

The GEMBOCHS database covers about 3200 distinct chemical species (spanning 86 elements of the periodic table); its core component is the current version of the SUPCRT92 database (Johnson et al., 1992; Shock, 1998), which covers about 1550 species (and 82 elements). Jewel, a GUI-driven software package that generates the application-specific datafiles, implements a large number of extrapolation algorithms, the core set of which are those encoded with the SUPCRT92 software package (Johnson et al., 1992). These include global- and critical-region equations of state and a dielectric formulation for H_2O (Johnson and Norton, 1991) that are explicitly integrated with equations of state for both aqueous solutes (Tanger and Helgeson, 1988; Shock et al., 1992) and minerals/gases (Helgeson et al., 1978).

In the present study, use of the GEMBOCHS database and Jewel software are almost exclusively restricted to those data and equations associated with the SUPCRT92 software package (Johnson et al., 1992; Shock, 1998).

Xtool

Xtool (Daveler, 1998) is s GUI-driven graphics utility for extracting and visualizing a broad range of output data from NUFT simulations. This versatile program reads time-history files, and from these creates user-specified x-y, contour, image, vector, and grid plots. In this study, Xtool has been used extensively to analyze simulation results, and to generate the 2-D color-contour plots contained in Figures 3-27.

In viewing these plots, it is important to recognize that property-value (color) gradients between adjacent cells represent center-to-center linear interpolation between the property values of each cell. This algorithm is appropriate and desirable except in certain instances where adjacent cells juxtapose extreme values. There are two such instances in the present set of simulations: shale-aquifer connections and—more importantly—connections between inner-domain cells and outer-boundary cells. In the latter case, these boundary cells, which necessarily impose fixed geochemical conditions and hydrostatic head (described below), are just 10^{-30} m wide, while the adjacent inner-domain cells are 25 m wide. Here, the linear interpolation algorithm is inappropriate because the property-value (color) gradient on the outer half of the inner-domain cells reflects influence of boundary-condition property values. This leads to incorrect color-contour representation of all property values in these outermost inner-domain cells; e.g., in the case of CO_2 immiscible saturation, it erroneously appears as if the immiscible CO_2 fluid does not exit the domain (Figure 3A). In the case of shale-aquifer connections, the problem is analogous, but less extreme. Again using CO_2 immiscible saturation as an example, it incorrectly appears as if there is a drop-off immediately beneath the shale cap rock because of the extreme difference in saturation between adjacent shale and aquifer cells (Figure 3B).

The simulation domain, time frame, and injection scenarios

All simulations are carried out within a single spatial domain, which represents the near-field sequestration environment at Sleipner, and over a single time frame, which encompasses equal-duration prograde and retrograde phases. In the common physical setting, an Utsira-like saline

aquifer (200 m thick) is confined by a shale cap rock (25 m), which itself is overlain by a thin confined saline aquifer (25 m) to facilitate evaluation of cap-rock performance. In the common 20-year time frame, an injection rate of 10^4 tons-CO_2/yr is first maintained for 10 years (prograde phase), then ramped down to zero over three months (prograde-retrograde transition phase), and finally maintained at zero for another 9.75 years (retrograde phase). This spatial domain and injection rate correspond to a one-meter-thick cross-section through and perpendicular to the actual 100-m screen length of CO_2 injection at Sleipner, where the integrated injection rate is 10^6 tons-CO_2/yr (Gregersen et al., 1998).

Three distinct injection scenarios—models XSH, CSH, and DSH—are evaluated in this context. Model XSH (Figure 2A), where no intra-aquifer shales are present, represents a homogeneous sand aquifer. Models CSH and DSH each contain four thin (3 m) intra-aquifer shales, separated from the cap rock and each other by 25 m. In model CSH (Figure 2B), these shales are laterally continuous and their assigned permeability (3 millidarcy) equates to a continuum representation of 100-micron fractures spaced roughly 30 m apart; i.e., it reflects that of microfractured thin shales. In model DSH (Figure 2C), these shales are laterally discontinuous and their assigned permeability (3 microdarcy; same as the cap rock) reflects typical shale integrity (Freeze and Cherry, 1979).

The base, top, and injection side (dotted red line in Figure 2) of the half-space domains are impermeable to flow. Constant hydrostatic head and geochemical conditions are maintained along the outer side (within the column of 10^{-30}-m-wide boundary cells), which is permeable to outward flow. These boundary cells serve as an infinite sink for outward migration of both the immiscible CO_2 and aqueous fluid phases. An ambient flow field has not been imposed within the saline aquifer, nor has any degree of tilt been imposed on the aquifer-cap rock interface.

Adopted hydrologic and compositional data

P-T conditions, porosities, and permeabilities assigned to the saline aquifer and shales are consistent with those reported for the Sleipner site whenever such data are available; in all other instances, reasonable estimates have been adopted (Table 1). At present, compositional data from Sleipner are either unavailable (fluid-rock analyses from shales and fluid analyses from the Utsira Formation) or proprietary (rock analysis from the Utsira Formation). Fortunately, we have obtained a report of mineral abundances from an Utsira-representative Miocene sand (courtesy of Tore Torp [Statoil] and Neils Springer [GEUS]), and a fluid analysis from the Utsira Formation 200 km north of Sleipner at Oseberg (Gregersen et al., 1998).

Mineral abundances adopted for the saline aquifer were modified from those given in the Miocene sand analysis. The primary adjustment was to eliminate the reported 5% calcite fraction (because the Utsira Formation is known to be highly unconsolidated; i.e., lacks carbonate cement) and to augment the feldspar fractions accordingly. In addition, because trace amounts of Fe/Mg-bearing mica (glauconite and biotite) have been reported for this formation (Gregersen et al., 1998), we have incorporated these in the form of 2% phlogopite; i.e., they are incorporated in terms of a representative Mg end-member component (Table 2).

Constraint of shale mineralogy is less straightforward, as there is a dearth of even proxy data. In lieu of such, we have adopted an estimate based on average shale compositions—60% clay minerals, 35% quartz, and 5% feldspar (Blatt et al., 1972)—and approximated the clay mineral fraction as a mixture of 50% muscovite and 10% clinochlore-14A (Mg-chlorite) (Table 2). This approximation preserves the typical $K_2O/(FeO+MgO)$ ratio of shales (Blatt et al., 1972), while permitting avoidance of the more realistic illite, smectite, and montmorillonite solid solutions, for which thermodynamic and kinetic data are lacking. Hence, here again, the actual Fe/Mg-bearing solid solution has been incorporated in terms of a representative Mg end-member component.

Ambient fluid composition adopted for both the saline aquifer and shales is based on the Oseberg analysis, but with several necessary modifications and additions (Table 3). The principal modification was to reduce reported Ca and Mg concentrations by 30% and reported bicarbonate concentration by 80%, which was required to achieve ambient undersaturation with respect to magnesite and calcite. This is justifiable, again based on the unconsolidated nature of the Utsira Formation. In addition, the ambient bicarbonate concentration—which in this reduced form agrees closely with that of seawater—is completely overwhelmed by the effect of CO_2 injection (whether or not it is reduced).

A second modification was to eliminate O_2(aq) and total Fe. The reported O_2(aq) value of 5 ppb cannot represent an *in situ* concentration; at 37°C/110 bars, it defines an equilibrated O_2(g) fugacity of roughly $10^{-3.8}$ (cf. the magnetite-hematite buffer under these conditions: $10^{-69.0}$). Hence, this value cannot be used to constrain the ambient oxidation state and dependent ferrous/ferric partitioning. A third modification was to eliminate Ba and Sr; these are trace components that have very minimal impact on simulation results. In terms of augmenting the Oseberg analysis, it was necessary to incorporate values for total aqueous silica and aluminum concentration; these were set by equilibration with the relevant mineral buffers (Table 3).

The adopted waste stream composition is pure CO_2, and it is injected under supercritical conditions (37°C, 111 bars) at the base of the saline aquifer. Under these P-T conditions, the injection CO_2 fugacity is 61.05 bars in the context of the adopted CO_2 fugacity coefficient (described below).

Our approach of incorporating Fe/Mg-bearing solid solutions as representative Mg end-member components was necessitated by removal of O_2(aq) and total Fe from the fluid analysis. Note that within the system Fe-C-O-H for the P-T conditions and injection CO_2 fugacity at Sleipner, siderite is stable over a wide range of O_2(g) fugacity—from the lower limit of H_2O stability ($10^{-83.2}$) to hematite-siderite equilibrium ($10^{-52.7}$)—roughly centered about the magnetite-hematite buffer ($10^{-69.0}$). Hence, incorporating Fe/Mg-bearing solid solutions as representative *Iron* end-member components would have little effect on the present study beyond replacing magnesite [$MgCO_3$] with siderite [$FeCO_3$] as the relevant calcite-group carbonate. (Reality, of course, lies within the middle ground of siderite-magnesite solid solutions.)

Adopted thermodynamic and kinetic data

The ambient equilibrium state and chemical evolution of the adopted aquifer-shale compositional environment at Sleipner (Tables 2-3) is represented using a Jewel-generated NUFT thermodynamic/kinetic datafile for the 10-component system K-Na-Ca-Mg-Al-Si-C-O-H-Cl over the P/T range 100 bars/20-90^{o}C. The equilibrium reference frame specified in this datafile, which includes 36 aqueous species, 2 gases, and 70 minerals, is derived almost entirely from those data—and using exclusively those equations of state—contained in the SUPCRT92 software package (Johnson et al., 1992) and the most recent associated database (Shock, 1998). Additional thermodynamic and kinetic data from a variety of sources were also adopted, as described below.

Adopted thermodynamic data beyond those contained within SUPCRT92 include Debye-Huckel ion-size parameters for aqueous solutes, a fugacity coefficient for CO_2(g), and reference-state properties for dawsonite. Ion-size parameters were taken from those assigned in GEMBOCHS-derived EQ3/6 datafiles (Johnson and Lundeen, 1994b), a CO_2(g) fugacity coefficient (0.55) for the relevant P-T conditions was taken from the universal gas activity coefficient chart (Garrels and Christ, 1965), and reference-state thermodynamic data for dawsonite were taken from Robie et al. (1978). In addition, data for three plagioclase solid-solution compositions (plag-Ab80, plag-Ab50, plag-Ab20) were added; these were derived using an ideal site-mixing model applied to SUPCRT92 data for albite and anorthite. Finally, dolomite and antigorite were suppressed, owing to the well-known (but poorly quantified) extreme discrepancy between low-temperature dissolution and precipitation rates of the former, and problematic stoichiometry of the latter.

The requisite kinetic data consist of reference-state mineral dissolution and precipitation rate constants, activation energies, and reactive specific surface areas. Because conditions within the intra-plume aqueous phase are uniformly acidic (both in space and time) within a narrow pH range (4-5.5), the dissolution rate constants and activation energies adopted are those relevant to these conditions (Table 4). Hence, in this application it is unnecessary to employ parallel rate laws that span the full pH spectrum. As is common practice, mineral precipitation rate constants are taken as equivalent to the corresponding dissolution rate constants, recognizing that this approximation is crude in some cases.

Although the reactive specific surface area of dissolving and precipitating minerals in the subsurface represents a critically important parameter, it is poorly quantified at present. In this study, we have adopted the following approach for assigning values to this key variable. For primary minerals in the saline aquifer, we first calculate the specific surface area for idealized spherical grains of reported Utsira size fraction: “fine to medium grained sand” (SACS, 2000); i.e., 0.25 mm grain diameter (based on the Udden-Wentworth size grade scale). Then, we apply to this initial value a scaling factor derived from experimentally observed factors of increase between specific surface areas of 100-micron spheres and BET-measured specific surface areas of 100-micron grains for quartz, albite, anorthite, K-feldspar, and muscovite (Knauss and Copenhaver, 1995; Knauss and Wolery, 1989, 1988, 1986; Stillings et al., 1996) (Table 4).

Scaling factors for primary minerals outside this group are assigned based on closest structural analogy (e.g., phlogopite is assigned the scaling factor observed for muscovite). In this highly porous and permeable saline aquifer, all surface area is considered to be available reactive surface area.

For primary minerals in the shales, the average size fraction of idealized spherical grains (mixture of very fine sand, silt, and clay particles) is taken to be 0.025 mm (silt), and the same scaling factor applied above is again used. Hence, mineral specific surface areas in the shales are ten times greater than those in the aquifer. However, within shales—unlike sand—only a small fraction of the *total* mineral surface area represents reactive surface area available to the aqueous phase; specifically, that fraction along and within diffusion distance of fracture walls, which—as a first approximation—we have taken to be 10%. As a result, *in this continuum model mineral reactive specific surface areas* in the shales are identical to those in the sand aquifer (Table 4).

For precipitation of potential secondary minerals in both the sand aquifer and shales, all *reactive* surface area of primary minerals is considered to represent available substrate; i.e., 100% and 10% of the *total* surface area per bulk volume for the sand aquifer and shales, respectively.

Simulation Results and Analysis

CO_2 migration/sequestration balance is most conveniently evaluated in terms of contributions from three interdependent yet conceptually distinct processes: CO_2 migration as an immiscible fluid phase, chemical interaction of this immiscible plume with formation waters, and plume interaction with formation minerals through this aqueous phase. The first process is directly linked to structural trapping, the second to solubility trapping and pH evolution, and the third to mineral trapping (and pH evolution). In this section, we evaluate and compare the relative effectiveness of these three trapping mechanisms for models XSH, CSH, and DSH during prograde and retrograde sequestration.

CO_2 immiscible migration and structural trapping

During prograde plume ascent in model XSH, the immiscible CO_2 fluid reaches the shale cap rock within 15 days and the domain boundary within 50 days; the plume cap, plume column, and residual saturation zone all attain near steady-state geometric configuration within one year (Figure 3A). At steady-state, CO_2 immiscible saturation in the core of the 20-m-wide plume column decreases from 0.22 at 25 m above the injection well to 0.13 just below the plume cap, where high saturation (0.50-0.58) is attained within the uppermost 25 m of the saline aquifer. Hence, a steep vertical gradient connects distinct saturation profiles in the plume column and cap. Laterally, the plume column and far-field environments are bridged by a 20-m-wide zone of residual saturation (0.05). This bridge represents the vertical wake of initial plume ascent to the shale cap rock, prior to subsequent lateral consolidation of the plume column. Here, the remnant immiscible CO_2 phase is no longer contiguous; hence, it is immobilized in terms of advective transport, but not with respect to diffusive or reactive processes. Subsequent prograde evolution

of CO_2 immiscible saturation is limited to a gradual increase in the plume cap, from values of 0.50-0.58 at one year to 0.60-0.67 after 10 years (Figure 3B).

Owing to 18% specific-volume expansion of the immiscible CO_2 fluid as it rises 200 m in the aquifer (20 bar pressure drop), once steady-state geometric configuration of the plume is attained, flow direction of the intra-plume aqueous phase is primarily downward within and slightly outward from the plume column, cap, and residual saturation zone during prograde sequestration. Advective velocities during this period are 10-100 cm/yr, and decrease with time. These velocities are on the order of those typically encountered in ambient saline aquifers.

Following the brief transition between prograde and retrograde regimes (10-10.25 years), the relict plume column rapidly infuses into the plume cap, leaving behind only residual saturation (0.05). After 9 months of retrograde outward migration, the plume cap has been reduced to a new steady-state thickness of 5 m (Figure 3C), within which CO_2 immiscible saturation has dropped to 0.52. After 20 years, plume-cap saturation has further diminished to 0.15 (Figure 3D). During this retrograde period, the aqueous-phase flow direction is directly opposite to that of the prograde regime—now primarily upward and slightly inward within the relict plume column, cap, and residual saturation zone—while flow velocities are similar in absolute magnitude.

During the prograde phase, roughly 85% (by mass) of the injected CO_2 within this near-field domain remains as an immiscible fluid phase. Hence, gravity segregation is the dominant migration process and structural trapping represents the most important potential trapping mechanism. While trapping within structural highs of the aquifer-shale interface cannot be evaluated in the present model (where this interface is flat), in the context of this 20-year simulation the 25-m (3 microdarcy) shale cap rock does provide a very secure seal. In particular, no CO_2 migrates completely through the 5 layers of 5-m-thick shale grid cells. Over the uppermost 20 m of shale, the maximum CO_2 immiscible saturation attained varies from 0.000015 in the upper 5 m to 0.0001 in the lowest 20 m – *and saturation is declining at 20 years*. In the 5 m of shale immediately overlying the aquifer, maximum saturation of 0.047 (less than the residual limit of 0.05) is attained at 14 years – *and declines thereafter to 0.042 at 20 years*. Hence, the 20-year performance of this 25 m shale cap rock is both excellent and improving with time.

The presence of thin intra-aquifer shales has a profound influence on immiscible-plume migration, although certain aspects of the process remain unchanged. For the case of laterally continuous microfractured shales (model CSH), the most obvious—and significant—effects are vertical bifurcation of the plume cap and a tremendous resultant increase in the volumetric extent of plume-aquifer interaction (Figure 4). When laterally discontinuous tight shales are imposed (model DSH), these effects are somewhat less pronounced; however, the lateral breaks lead to a unique and significant spatial recursion of focused vertical CO_2 migration paths and lateral saturation gradients throughout the near-field domain (Figure 5).

In both models, the evolution of maximum CO_2 immiscible saturation within the aquifer, attainment of steady state plume configuration, general progression of retrograde plume dispersal, and cap-rock performance are all similar to the homogeneous aquifer case (cf. Figures 3-5). In model CSH, maximum steady-state CO_2 immiscible saturation within the four relatively permeable intra-aquifer shales (from 0.42 in the lowest to 0.25 in the highest) is attained within 5-6 years during prograde sequestration. During the first year of the retrograde phase, saturation within all four plummets to the residual limit of 0.05, and by 18 years has been reduced to zero (Figure 4D). This elimination of immiscible CO_2 reflects its eventual complete consumption by carbonate-precipitating fluid-mineral reactions (described below). In model DSH, saturation in the four relatively impermeable shales increases slowly throughout the prograde regime (reaching maximum values between 0.06 and 0.10). It then decreases slowly throughout the retrograde phase, eventually reaching zero at 18 years (Figure 5D), again as result of complete consumption by carbonate precipitation.

Most importantly, the presence of intra-aquifer shales in both CSH and DSH creates the potential for sub-cap rock structural trapping and—by greatly expanding the extent of plume-aquifer interaction—significantly increases the effectiveness of solubility and mineral trapping.

CO_2 immiscible saturation profiles from models XSH, CSH, and DSH at 3 years are shown together with the corresponding seismic profile of immiscible CO_2 accumulations at Sleipner in Figure 6. Comparison of these four images suggests that the spatial distribution of such accumulations at Sleipner requires the presence of thin intra-aquifer shales in the upper half of Utsira Formation. Moreover, close correspondence of model CSH and the seismic data suggests that these shales are predominantly contiguous laterally, but have significant microfracture permeability. The presence of lateral facies changes (to sand) would result in a much greater proportion of injected CO_2 reaching the cap rock after 3 years, as in model DSH, where the lateral breaks are actually quite restricted (10-25 m in width) relative to typical field settings.

All solubility and mineral trapping mechanisms are catalyzed by plume-aquifer interaction. Hence, the space-time evolution of these geochemical processes directly mirrors that of CO_2 immiscible saturation during prograde sequestration (Figures 3A-B, 4A-B, and 5A-B). Moreover, the residual saturation (0.05) left in the prograde plume's wake (figures 3D, 4D, and 5D) permits continued effectiveness of solubility and mineral trapping during retrograde sequestration.

Solubility trapping and pH evolution

As the immiscible CO_2 plume interacts with saline formation waters, the fundamental effect on the latter is a dramatic increase in total carbon concentration, primarily as $CO_2(aq)$ and HCO_3^- (solubility trapping), and a substantial decrease in pH (the critical forerunner of all mineral trapping mechanisms). The coupled reaction can be expressed as:

$$CO_2(g) + H_2O \leftrightarrow CO_2(aq) + H_2O \leftrightarrow HCO_3^- + H^+ \quad . \qquad (1)$$

During initial plume ascent to the shale cap rock in model XSH, intra-plume formation waters immediately equilibrate with CO_2(g), creating a coincident plume of CO_2 aqueous saturation. For this chemical system, injection CO_2(g) fugacity, and vertical pressure gradient, composite CO_2 aqueous solubility varies from about 1.2 molal near the well to about 1.1 molal at the aquifer-cap rock interface (Figure 7A). This aqueous-saturation plume persists throughout the prograde regime (Figure 7B) *as well as the retrograde phase* (Figure 7C), owing to residual saturation left in the wake of retrograde plume dispersal (Figure 3D). The spatial gradient that bridges this 1.1-1.2 molal concentration and the small ambient value is uniformly steep. During the prograde regime for model XSH, solubility trapping sequesters about 15% of the injected CO_2 mass within this near-field domain.

Although this *percentage* is not appreciably increased by the insertion of intra-aquifer shales (because it represents a solubility limit for the specified chemical conditions), the *relative effectiveness* of solubility trapping is in fact significantly increased (Figures 8-9). By retarding vertical and promoting lateral migration of the immiscible plume, these shales delay the exit of injected immiscible CO_2 from the near field environment and expand tremendously both the volumetric extent of plume-aquifer interaction and the areal extent of plume-formation water interaction. The net result is a dramatic increase in the total mass of injected CO_2 trapped in the near-field aqueous phase and a significant increase in the specific mass so-trapped per mass of immiscible CO_2.

In models CSH and DSH, the total mass of solubility-trapped CO_2 in the near field exceeds that for model XSH by a factor of 3.2 and 1.4, respectively—roughly equivalent to the factor-of-increase in areal extent of CO_2 aqueous saturation (cf. Figures 7-9). These large increases reflect the retarded exit of injected immiscible CO_2 from the near-field domain. In addition—and more significantly—after 10 years of prograde injection the mass ratio of solubility-trapped to immiscible-phase CO_2 within this near-field domain is 32 and 44% larger in models CSH and DSH, respectively, than in model XSH. These increases mark the improved relative effectiveness of solubility trapping in the intra-aquifer shale environment owing to lower domain-averaged CO_2 immiscible saturation within the plume, which is equivalent to increasing surface area of the plume-formation water interface.

The relative effectiveness of solubility trapping also has an important compositional dependence on formation waters. Because aqueous solubility of a gas generally decreases with increasing ionic strength at constant P-T, owing to the experimentally-observed “salting-out-effect” (Garrels and Christ, 1965), solubility trapping will become less effective with increasing salinity of the ambient fluid phase. As a result, the relative effectiveness of solubility trapping will progressively decrease as formation waters vary from dilute to saline to brine. This transition is accounted for in simulation studies by adoption of an appropriate activity-coefficient model for dissolved-gas aqueous solutes (e.g., Drummond, 1981).

CO_2 aqueous solubility has dropped below even the ambient value within all intra-aquifer shales of both models CHS and DSH after 10 years of retrograde sequestration (Figures 8C and 9C).

This reflects complete consumption of CO_2 from the intra-plume aqueous phase (and therefore from the immiscible plume itself) through carbonate precipitation.

Evolution of aqueous-phase pH within the immiscible CO_2 plume represents a balance between two opposing processes: equilibrium aqueous solubility of influx CO_2, which dramatically decreases pH (reaction 1), and dependent kinetic dissolution of silicate minerals (discussed below), which increases it. The first of these dominates the battle, lowering pH from the ambient value of 7.1 to roughly 4.5 throughout the plume column, cap, and residual saturation zone of model XSH during initial plume ascent (Figure 10A). However, continuous silicate dissolution within these regions throughout prograde sequestration imprints upon this imposed background value a small but continuous increase from 4.5 to 4.9 in the plume column and residual saturation zone, and from 4.5 to 5.2 in the plume cap (Figure 10B). During retrograde sequestration, persistent residual CO_2 saturation maintains the low background pH, which continues to drive silicate dissolution; hence, pH continues to rise slowly, reaching about 5.3 throughout the plume at 20 years (Figure 10C). The spatial gradient bridging low-pH fluids within the plume and near-neutral outlying solutions is uniformly steep.

Insertion of intra-aquifer shales has little influence on the general progression of pH evolution observed in the homogeneous saline aquifer case, but it does impose two very significant modifications to this evolution. The first and most important of these is the anticipated effect of greatly expanding the volumetric extent of low-pH fluids within the saline aquifer (Figures 11-12). This significantly impacts mineral trapping because it similarly expands the volume of silicate minerals under acid attack, and therefore the effective source region of potential carbonate-forming cations. The second modification pertains only to model DSH. Here, the unique spatial recursion of focused vertical CO_2 migration (Figure 5) leads to similar recursion of steep lateral gradients in CO_2 aqueous solubility and pH (Figures 9 and 12). These too play an important role in mineral trapping.

Relatively high pH values within the intra-aquifer shales of both models CSH and DSH after 10 years of retrograde sequestration (Figures 11C and 12C) are attained rapidly between 16 and 18 years as the final vestige of CO_2 is consumed by local carbonate precipitation.

Mineral Trapping

Geologic CO_2 sequestration in the form of mineral trapping offers three distinct advantages over the structural and solubility mechanisms: storage capacity is maximized (carbonate minerals representing the densest phase), mobility is minimized (effectively eliminated), and aquifer/shale permeability is reduced (improving containment of the immiscible and dissolved aqueous fractions). In saline aquifers, mineral trapping will occur primarily in the form of dawsonite [$NaAlCO_3(OH)_2$] and the calcite-group carbonates, most significantly siderite [$FeCO_3$], magnesite [$MgCO_3$], calcite [$CaCO_3$], and their solid solutions. In the present model, we evaluate the contributions of dawsonite, magnesite (representing combined siderite/magnesite), and calcite.

As detailed above, the intra-plume aqueous phase is both highly acidic and CO_2 saturated. The low pH catalyzes silicate dissolution, releasing carbonate-forming cations (Mg, Ca, Na, and Al in this case) to the CO_2-saturated fluid, and thereby setting the stage for subsequent mineral trapping. Carbonate precipitation occurs within three distinct regions of the near-field environment: within the saline aquifer in the plume cap, column, and residual saturation zone (dawsonite > magnesite), along lateral margins of the plume cap and residual saturation zone (magnesite > calcite), and—most importantly—within cap-rock and intra-aquifer shales (magnesite >> dawsonite > calcite). Magnesite and calcite precipitate by identical mechanisms that vary between these regions, while the unique process of dawsonite precipitation is uniform in the aquifer and shale environments.

Dawsonite precipitation within the aquifer and shales

Dawsonite precipitation is catalyzed by high ambient Na concentration, plume-induced CO_2 aqueous saturation, and acid-induced kinetic dissolution of K-feldspar. The coupled reaction in both the aquifer and shale environment can be expressed as:

$$\underset{\text{K-feldspar}}{KAlSi_3O_8} + Na^+ + CO_2(aq) + H_2O \leftrightarrow \underset{\text{dawsonite}}{NaAlCO_3(OH)_2} + 3\,\underset{\text{qtz/chal/crist}}{SiO_2} + K^+ \quad . \quad (2)$$

The adopted reference-state dissolution rate constant of K-feldspar is 10^3 times slower than the corresponding dawsonite precipitation rate constant, but exceeds by a factor of 10^3-10^4 the corresponding precipitation rate constants of the three most stable silica polymorphs (quartz, chalcedony, and cristobalite). Hence, in the presence of excess aqueous Na and CO_2, K-feldspar dissolution is the rate-limiting step, and aqueous silica concentrations quickly reach and maintain supersaturation with respect to all three silica polymorphs, which precipitate together with dawsonite.

Because K-feldspar dissolution is represented kinetically, in contrast to the equilibrium treatment of CO_2(aq) saturation, initial dawsonite precipitation within the aquifer and shale cap rock of model XSH is not coincident with initial immiscible plume ascent. Dawsonite precipitation is first realized within the shale cap rock (basal 5 m layer only) at about 0.25 years, and within the aquifer (throughout the plume cap, column, and residual saturation zone) at about 0.5 years. Once initiated, this precipitation persists throughout the prograde *and retrograde* phases, as dawsonite volume fractions approach 0.002 (Figure 13). Reaction (2) proceeds from left to right with an increase in solid-phase volume that varies from 17% (quartz and chalcedony) to 25.4% (cristobalite). However, because K-feldspar comprises only 6.5% of the initial aquifer volume, and because the reaction proceeds kinetically, the time-integrated reduction in aquifer porosity after 20 years amounts to less than 0.02%.

The introduction of intra-aquifer shales dramatically increases aggregate dawsonite concentration in the near-field environment, while volume-averaged concentrations remain unchanged (Figures 14-15). The composite mass of dawsonite precipitated within models CSH and DSH exceeds by a factor of 2.9 and 1.9, respectively, that precipitated in model XSH. This increase is almost

wholly accounted for by increased precipitation in the aquifer itself, as dawsonite concentrations in the shale cap rock are nearly identical in the three models, and precipitation within intra-aquifer shales is relatively minor (Figures 14-15).

Dawsonite precipitation is unique among mineral-trapping mechanisms in that it is fundamentally catalyzed by the composition of ambient formation waters—the high Na concentration of saline fluids (here, 0.45 molal). Hence, pervasive dawsonite cement is very likely to form as a result of CO_2 injection into *any* saline aquifer that contains Al-bearing silicates (in particular, K-feldspar). In fact, there is a natural analog for this process: the presence of widespread dawsonite cement in the Bowen-Gunnedah-Sydney Basin, Eastern Australia, which has been interpreted to reflect magmatic CO_2 seepage on a continental scale (Baker et al., 1995).

Magnesite/calcite precipitation within the aquifer

Calcite-group carbonates precipitate via distinct mechanisms within the plume cap and along lateral margins of the plume cap and residual saturation zone. However, both processes can be described in the context of the following general hydrolysis reaction:

$$\underset{\substack{\text{calcite-group}\\ \text{carbonate}}}{\underline{MCO_3}} + 2\,H^+ \leftrightarrow M^{+2} + CO_2(aq) + H_2O \quad , \qquad (3)$$

for which

$$\log K = \log a_{M+2} + \log a_{CO2(aq)} + 2\,pH \quad . \qquad (4)$$

As noted above, once the immiscible CO_2 plume attains steady state configuration, CO_2(aq) activity and pH are maintained at nearly constant values within the intra-plume aqueous phase during both prograde and retrograde sequestration. Aqueous-phase equilibration with CO_2(g) promotes carbonate precipitation, while the acidic conditions favor carbonate dissolution. In the context of this near-constant intra-plume contribution of [$\log a_{CO2(aq)} + 2\,pH$] to log Q for reaction (4), typical *ambient* saline-aquifer M^{+2} concentrations—such as those for Mg^{+2} and Ca^{+2} in this model—are insufficient to realize saturation with respect to any MCO_3.

However, during prograde sequestration intra-plume aqueous M^{+2} concentrations increase linearly owing to continuous silicate dissolution. For a specific M^{+2}, the rate of local concentration increase depends on several factors, most importantly the abundance, M-concentration, dissolution rate constant, and specific surface area of ambient M-bearing formation minerals—but also the magnitude of CO_2 immiscible saturation. Within the adopted model of saline-aquifer mineralogy (Table 2), Mg^{+2} is available exclusively from phlogopite (2% of the solid-phase volume, 3 moles-Mg/mole-phlogopite), while Ca^{+2} is available exclusively from plag-Ab80 (5% of the solid-phase volume, 0.2 moles-Ca/mole-plag-Ab80). Hence, the source reservoir for Mg is roughly 6 times that of Ca. Moreover, the adopted specific surface

area of phlogopite exceeds that of plag-Ab80 by a factor of almost 15, while its reference-state dissolution rate constant is only 30% smaller. As a result, in this model the bulk release rate for Mg from silicate dissolution will be roughly 60-70 times that of Ca. This much larger release rate—together with the larger background concentration of Mg (factor of 2.4, Table 3)—strongly suggests that aqueous saturation with respect to magnesite will obtain more readily than that with respect to calcite, despite slightly higher solubility of the former.

As intra-plume aqueous M^{+2} concentrations (and log Q for reaction 4) increase with time (Mg >> Ca in this model), there are two environments where evolving conditions lead to MCO_3 precipitation: the plume cap and lateral margins of the plume cap and residual saturation zone.

Precipitation along lateral plume margins

While aqueous M^{+2} concentrations are increasing throughout the plume during prograde sequestration, the aqueous-phase flow direction is primarily downward and slightly outward. As this M^{+2}-charged aqueous phase migrates across the plume boundary and into the ambient saline aquifer environment in model XSH, it crosses steep spatial gradients in pH and CO_2 aqueous solubility (Figures 7 and 10). The magnitude of this pH increase (which favors MCO_3 precipitation) exceeds significantly that in CO_2 aqueous solubility decrease (which favors MCO_3 dissolution). As a result, *for all MCO_3* there exists a background spatial gradient in the [log $a_{CO2(aq)}$ + 2 pH] contribution to log Q for equation (4) that is highly conducive to their precipitation along this flow path. As a result, MCO_3 precipitation from the migrating aqueous phase will occur as soon as sufficient M^{+2} concentration is realized through silicate dissolution within the plume.

Precipitation of this lateral carbonate "rind" begins along an outer shell (after about 0.25 years in model XSH), which marks the initial achievement of saturation-sufficient M^{+2} concentration. Then, as the M^{+2} concentration of migrating fluids continues to increase with time, this carbonate rind becomes more concentrated and grows primarily upward and slightly inward from the outer shell—opposite to the flow direction (Figures 16A and 16B).

During retrograde sequestration, aqueous-phase flow directions are reversed; i.e., fluids are now moving primarily upwards, slightly inwards, and into the remnant residual saturation zone. Hence, a carbonate-undersaturated aqueous phase is now migrating through the prograde rind zone and across a gradient in [log $a_{CO2(aq)}$ + 2 pH] that favors carbonate dissolution. However, carbonate precipitation becomes increasingly favored along this traverse as M^{+2} (here, Mg^{+2}) concentrations increase rapidly from magnesite dissolution along the prograde rind's outer shell and continued phlogopite dissolution. In fact, magnesite saturation obtains and its precipitation begins before the prograde inner shell is reached—and it continues beyond this point. Hence, the net result is slow migration of the prograde carbonate rind upwards and inward during retrograde sequestration while its concentration increases (Figure 16C).

The influence of intra-aquifer shales on development of carbonate rind is highly dependent on their lateral continuity. When such continuity exists, as in model CSH, the presence of such

shales has very little influence other than vertical restriction of rind development to beneath the lowest shale inter-bed (Figure 17). Because the aqueous-phase primary flow directions are downward (prograde regime) and upward (retrograde phase) in both XSH and CSH (below the lowest shale inter-bed), the total mass of rind-precipitated magnesite is nearly identical in both models.

In contrast, lateral discontinuity of intra-aquifer shales, as imposed in model DSH, has two very dramatic effects on the extent and distribution of carbonate rind formation. First, spatially recursive lateral gradients in CO_2 aqueous solubility (Figure 9) and pH (Figure 12)—which develop around each column of focused vertical CO_2 migration (Figure 5)—lead to similarly recursive precipitation of carbonate rinds. During the prograde phase, they precipitate as "blooms" just above and to either side of each lateral break (Figure 18A and 18B). During the retrograde regime, these blooms migrate away from the breaks, coalesce (from either side), and appear as mounds above each interior shale segment (Figure 18C). The second dramatic effect of lateral discontinuity is to create a highly irregular outer boundary to the residual saturation zone; this flattens the otherwise steep CO_2 aqueous solubility and pH gradients, leading to precipitation of a much broader carbonate rind that delimits lateral plume extent (cf. Figures 16C, 17C, and 18C). As a result of these two effects, the total mass of intra-aquifer magnesite precipitation is model DSH is 75% greater than in models XSH and CSH.

Precipitation of calcite along lateral plume margins is genetically identical to that of magnesite. However, the small source reservoir and slow release rate for Ca (relative to Mg) in this model delay the appearance (until the retrograde regime) and minimize the concentration of calcite (relative to magnesite) within lateral carbonate rind (Figures 19-21).

Precipitation within the plume cap

As mentioned above, CO_2 immiscible saturation plays a key role in the evolution of intra-plume aqueous M^{+2} concentrations. In particular, for a given rate of M^{+2} hydrolysis from mineral dissolution, the increase in (bulk) aqueous M^{+2} concentration is inversely proportional to thickness of the aqueous wetting fluid; i.e., directly *proportional* to CO_2 immiscible saturation. Hence, aqueous M^{+2} concentrations will increase most rapidly within the plume cap, where CO_2 immiscible saturation is 3-4 times larger than within the plume column. As a result, if MCO_3 precipitation does in fact occur *within* the plume (i.e., sufficient M^{+2} concentrations are in fact reached), it will be localized within this narrow 25-m cap zone. Moreover, because immiscible saturation reaches a maximum at the cap-rock interface, this is where MCO_3 cementation will initiate, then expand downward into the aquifer.

In model XSH, magnesite saturation obtains at this interface after about 8 years, and a magnesite cementation zone grows downward henceforth throughout the prograde and retrograde regimes (Figures 16B and 16C). The identical process occurs in model CSH, where this roof-downward cementation develops beneath the shale cap rock and all intra-aquifer shales (Figure 17C), and in model DSH, where it develops only beneath the cap rock, but here to the greatest extent observed in the three models (Figure 18C).

Porosity evolution within the near-field aquifer environment during prograde and retrograde sequestration reflects the integrated effect of the mineral dissolution/precipitation processes examined above. Although dawsonite precipitation (reaction 2) dominates this evolution in all three models, the influence of magnesite precipitation within the plume cap (reaction 3), and magnesite/calcite precipitation along plume margins (reaction 3) is readily distinguished (Figures 22-24). The early porosity increase, primarily due to K-feldspar dissolution, is eventually outstripped by dawsonite-plus-silica precipitation throughout the plume – augmented by magnesite precipitation in the plume cap. This latter effect leads to maximum aquifer porosity reduction (about 0.2%) immediately beneath the shale cap rock and shale inter-beds in all models.

In summary, during prograde sequestration—when the intra-plume aqueous phase migrates downward and outward from the plume—carbonate precipitation provides an inward-growing seal along lateral plume margins and a downward-growing seal from the cap-rock interface. During the retrograde phase—when flow directions are reversed and ambient formation fluids are now entering the residual saturation zone—carbonate concentration within the prograde lateral rind increases as it migrates upwards and inward, while roof-downward cementation continues. Hence, mineral trapping through these two mechanisms, while volumetrically negligible, has a potentially large strategic impact in terms of isolating both prograde plume migration and retrograde residual saturation.

Magnesite precipitation within intra-aquifer and cap-rock shales

Magnesite precipitation within the cap-rock shale of model XSH occurs within a very different chemical environment than discussed above for carbonate precipitation within the saline aquifer. Here, the acidic, CO_2-saturated, intra-plume aqueous phase moves by slow advection along microfractures and by extremely slow diffusion across microfracture walls and into shale matrix blocks. Along these migration paths, it interacts with a clay-mineral-dominated solid-phase assemblage, whose bulk Fe/Mg concentration is much greater than that of the underlying aquifer. Incipient dissolution of Fe/Mg-bearing clay minerals (here represented by Mg-chlorite) rapidly increases aqueous Fe/Mg concentration (here, Mg), which leads to saturation with respect to and therefore precipitation of Fe/Mg carbonates (here, magnesite). Hence, in shales the rate ratio of mineral dissolution/precipitation to advection/diffusion is much larger than in the underlying aquifer *and* there is a much greater solid-phase concentration of Fe/Mg that can be converted from silicates to carbonates. This setting is highly conducive to Fe/Mg-carbonate cementation.

For the present set of simulations, the fundamental coupled reaction by which magnesite precipitates in the shale environment can be expressed as:

$$\underset{\text{K-feldspar}}{KAlSi_3O_8} + 2.5\ \underset{\text{Mg-chlorite}}{Mg_5Al_2Si_3O_{10}(OH)_8} + 12.5\ CO_2(aq)$$

$$\leftrightarrow$$

$$\underset{\text{muscovite}}{KAl_3Si_3O_{10}(OH)_2} + 1.5\ \underset{\text{kaolinite}}{Al_2Si_2O_5(OH)_4} + 12.5\ \underset{\text{magnesite}}{MgCO_3} + 4.5\ \underset{\text{qtz/chal}}{SiO_2} + 6\ H_2O \quad , \qquad (5)$$

whose stoichiometry follows from the relative magnitude of molar volumes and of dissolution/precipitation volume fractions among the participating solids. Reaction (5) proceeds to the right with a solid-phase volume increase of roughly 18.5% (magnesite accounts for 47 volume percent of the product assemblage); when applied to the original volume fraction of K-feldspar and Mg-chlorite (0.1425), this 18.5% expansion yields a new volume fraction of 0.1688 (increase of 0.0263). Hence, if reaction (5) proceeded to completion, shale porosity would be decreased from 0.05 to 0. 0237—less than half its original value. However, the observed decrease in model XSH, from 0.05 to 0.046, indicates that over the 20-year simulation, this kinetic reaction has only attained 15% completion (which agrees with the observed decrease in Mg-chlorite and K-feldspar volume fractions).

Magnesite precipitation within the shale cap rock of model XSH is limited to the basal 5 m, where its volume-fraction concentration approaches 0.01 after 20 years (Figure 25). This concentration is 20 times larger than that attained in either the plume cap or lateral plume margins within the aquifer (cf., Figures 16 and 25). *In fact, magnesite precipitation within the lower 5 m of the shale cap rock accounts for 55% of the total CO_2 mass precipitated as carbonate in model XSH.*

The presence of intra-aquifer shales dramatically enhances the effectiveness of intra-shale mineral trapping. Within the shale cap rock of models CSH and DSH, magnesite precipitation is again limited to the basal 5 m, where its volume-fraction concentration again approaches 0.01. However, similar concentrations are now attained in all of the intra-aquifer shales of both models (Figures 26-27), where continuous CO_2 consumption through prograde/retrograde magnesite precipitation (reaction 5) exhausts local immiscible-plume and aqueous concentrations after 18 years (Figures 4D, 5D, 8C, and 9C). As a result, in models CSH and DSH the total amount of CO_2 trapped by intra-shale magnesite precipitation—and the total amount trapped from *all* carbonate precipitation—exceeds that of model XSH by factors of 3.0 and 1.8, respectively. Nevertheless, even in model CSH mineral trapping in the near-field domain accounts for less than 0.3% of the injected CO_2 mass.

While this contribution is negligible volumetrically, it is critical strategically in terms of improving isolation performance. Any shale permeability is fracture permeability, and virtually

all intra-shale carbonate precipitation (as described above) will be at the expense of fracture porosity. As a result, volumetrically minor intra-shale carbonate precipitation will have a disproportionately large sealing effect with respect to fracture permeability; i.e., this carbonate sealing will therefore serve to increase—significantly—the integrity of shale cap rocks.

Porosity evolution within the shale cap rock of models XSH, CSH, and DSH illustrates this concept (Figures 28-30). The slight increase in porosity in the upper 20 m reflects undersaturation of the ambient aqueous phase with respect to K-feldspar (which may or may not reflect reality) and lack of CO_2 encroachment. Most significantly, such dissolution is completely overridden by carbonate-dominated cementation of fracture porosity in the basal 5 m, where magnesite accounts for 47 volume percent of the product assemblage (reaction 5).
Here, porosity reduction from 0.05 to 0.046 translates to an estimated 22% reduction in permeability, from 3 to 2.33 microdarcy, owing to the cubic dependence of relative permeability evolution on that of relative porosity. Moreover, this *continuum-based* estimate severely underestimates the actual reduction in flow permeability. Further, *magnesite precipitation within cap-rock microfractures will continue throughout retrograde sequestration until either fracture porosity is sealed or the underlying immiscible CO_2 phase is exhausted*.

Benefits and Applications

Reactive transport modeling provides a unique means of addressing—quantitatively—the fundamental questions posed above regarding the processes and effectiveness of geologic CO_2 sequestration in saline aquifers. Specifically, the simulation results and analysis presented here have quantified immiscible-plume migration paths, the isolation performance of a typical shale cap rock, the influence of intra-aquifer permeability structure, and the relative effectiveness of structural, solubility, and mineral trapping—all within the contrasting environments of prograde and retrograde sequestration. Moreover, these results and analysis reveal fundamental structural, hydrologic, and compositional constraints on achieving optimal isolation performance.

Intra-aquifer permeability structure exerts the predominant control on immiscible CO_2 migration paths and the relative effectiveness of solubility and mineral trapping mechanisms, while cap-rock integrity represents the single most important variable influencing long-term storage security. By retarding vertical and promoting lateral migration of the immiscible CO_2 plume, thin intra-aquifer shales delay its net outward migration, significantly expand the volumetric extent of plume-aquifer interaction, and thereby dramatically increase the effectiveness of intra-plume solubility and mineral trapping mechanisms. A 25-m-thick shale cap rock having typical-shale hydrologic properties provides an extremely secure barrier to continued vertical migration of the underlying immiscible CO_2 plume.

Within the near-field sequestration environment of the present model, roughly 85% of injected CO_2 mass remains and migrates as an immiscible fluid phase, approximately 15% dissolves into formation waters, and less than 1% precipitates as carbonate minerals. This breakdown holds for

whether or not intra-aquifer shales are present, because the 15% aqueous dissolution represents a compositional-dependant solubility limit. However, the presence of intra-aquifer shales increases the *total mass* of solubility-trapped CO_2 in the near field by a factor of 1.4-3.2 over the homogeneous-aquifer case, and increases the mass percentage of mineral-trapped CO_2 by a factor of 1.8-2.8 (from 0.092% to 0.165-0.257%).

These data define relative effectiveness—*from a mass (or volume) perspective*—of the fundamental trapping mechanisms: structural >> solubility >> mineral. However, it is important to recognize that among these, only mineral trapping is *directly* enhanced during retrograde sequestration. Moreover, *the relative effectiveness of mineral trapping is far more accurately measured by its impact on immiscible CO_2 migration, rather than on a mass (or volume) basis.*

Although volumetrically negligible, mineral trapping is strategically critical in that it significantly increases integrity of the cap-rock seal and bounds the lateral extent of plume migration. Specifically, the shale cap rock is cemented from the aquifer-shale interface upwards by precipitation of a magnesite-dominated assemblage (reaction 5) that reduces microfracture porosity and permeability by *at least* 8 and 22%, respectively, over 20 years. *As long as the immiscible CO_2 plume remains beneath the aquifer-shale interface, this carbonate cementation of cap-rock microfracture porosity will continue throughout retrograde sequestration until such porosity is completely sealed.* Hence, integrity of the cap-rock will be continuously improved. In addition, the aquifer itself is cemented from the aquifer-shale interface downwards by magnesite precipitation (reaction 3), laterally by magnesite/calcite precipitation within carbonate rind (reaction 3), and throughout by dawsonite precipitation (reaction 2). These three processes of aquifer cementation will also be continuous throughout the retrograde regime as long as the source region of carbonate-forming cations is not exhausted by continued mineral dissolution.

The *actual* effectiveness of mineral trapping depends on the initial concentration of carbonate-forming cations (and thermodynamic/kinetic properties of their host minerals) within the target aquifer, shale cap rock, and inter-bedded shales. From an average-concentration standpoint (based on bulk-rock oxide analyses), the most important such cations—both in unconsolidated sand aquifers and in shales—are $Fe^{+2/+3} > Mg^{+2} > Ca^{+2}$ (Blatt et al., 1972). However, owing to their preponderance of clay minerals, shales are at least 2-3 times richer than such aquifers in average Fe_2O_3+FeO+MgO abundance (Blatt et al., 1972). Ca concentrations are relatively small in both environments (although the opposite is true for many *cemented* sandstones); hence, in Sleipner-like settings, calcite is expected to play a minor role in mineral trapping relative to siderite, magnesite, and their solid solutions.

Based on our simulations and analysis, optimal sequestration performance within a Sleipner-like setting (unconsolidated saline aquifer with a shale cap rock) requires all of the following:

- A laterally extensive and continuous shale cap rock having at least typical-shale hydrologic properties (porosity/permeability) and 25-m thickness to prohibit vertical migration of immiscible CO_2; decreased porosity/permeability and increased thickness

are desirable.

- Multiple inter-bedded thin shale (or hydrologically-equivalent) units to maximize the volumetric extent of plume-aquifer interaction, delay the outward migration of immiscible CO_2 from the near-field environment, and create the potential for sub-cap structural trapping.
- Moderate salinity: high enough to promote dawsonite cementation throughout the plume (reaction 2), but not so concentrated as to significantly reduce the effectiveness of solubility trapping (reaction 1).
- High concentrations of detrital Fe-Mg micas/oxides within the aquifer to maximize carbonate cementation within the plume cap and along lateral plume margins (reaction 3)
- High concentrations of Fe/Mg clays within intra-aquifer and especially cap-rock shales to maximize local carbonate cementation (reaction 5) and thereby improve integrity of these key barriers to vertical migration of immiscible CO_2.

Future Activities

Geologic CO_2 sequestration poses an integrated set of fascinating coupled-process problems that can only be solved using the reactive transport modeling approach. In this study, we have demonstrated the utility of both this approach and our simulation capabilities. Our current focus is on improving these capabilities and expanding our scope of applications within the geologic sequestration arena.

There are two distinct yet integrated components to model improvement: development and implementation of new capabilities to fill identified voids, and overall model refinement though benchmarking against experimental and field data. Here, the former component includes explicit account of impurities in the CO_2 waste stream (e.g., CH_4, H_2S, NO_x, SO_x), solubility of formation waters into the "immiscible" CO_2 plume, an equation of state for saline fluids, and continuous solid-solution compositions (carbonates, feldspars, micas, clays). The latter includes carrying out laboratory experiments designed to investigate certain model predictions, such as plug-flow reactor and batch experiments designed to replicate predicted carbonate cementation above and below the aquifer-cap rock interface. It also includes modeling available field data from relevant sites, such as those from Sleipner in the present study, and we are actively seeking industrial collaborators in this pursuit.

We are also expanding our application scope to include other geologic settings proposed for CO_2 sequestration. These include both pure isolation targets, such as a broad range of saline aquifer/cap rock environments, and those where CO_2 isolation represents an ancillary benefit: petroleum reservoirs where CO_2 flooding has become an important method of enhanced oil recovery (EOR).

Although the simulations and analysis presented here are broadly relevant to CO_2 sequestration in the general saline-aquifer environment, strictly speaking they are directly applicable only to

the specific conditions evaluated: pure CO_2 injected into a shale-capped impure quartz sand plus-or-minus thin shale inter-beds. Many important variants of this baseline study require explicit treatment, most importantly those in composition (waste stream, aquifer, formation waters, cap rock), P-T conditions (aquifer depth and thickness), CO_2 injection rate, and spatial scale (expanded to address both near- and far-field effects). In addition, explicit account of aquifer-cap rock topography and ambient flow fields—as well as use of radial-3D spatial domains—are required to address up-dip immiscible CO_2 migration and structural trapping. These features have been implemented in our modeling capability, but not yet applied to simulations of geologic CO_2 sequestration.

Use of this capability to investigate the sequestration potential of EOR methods represents an exciting extension of our work on saline aquifers. While such extension requires incorporating appropriate equations of state for the relevant hydrocarbons, this will enable us to quantify the dependence of net CO_2 sequestration on key reservoir and hydrocarbon properties. Although such dependence is of obvious and great importance both within and beyond the petroleum industry, it presently awaits quantification.

References

Baker, J.C., Bai, G.P., Hamilton, P.J., Golding, S.D., and Keene, J.B., 1995, Continental-scale magmatic carbon-dioxide seepage recorded by dawsonite in the Bowen-Gunnedah-Sydney Basin,, Eastern Australia: J. Sed. Res., Sec. A – Sed. Petrol. Processes, v. 65, n. 3., p. 522-530.

Bethke, C.M., 1994, The Geochemist's Workbench (Version 2.0): A user's guide to Rxn, Act2, Tact, React, and Gtplot: Hydrogeology Program, Univ. Ill., 213 p.

Blatt, H., Middleton. G., and Murray, R., 1972, Origin of Sedimentary Rocks: Prentice-Hall, Englewood Cliffs, N.J., 634 p.

Blum, A.E., and Stillings, L.L., 1995, Feldspar dissolution kinetics: in White, A.F., and Brantley, S.L. (Eds.), Chemical Weathering Rates of Silicate Minerals: Rev. Min., v. 31, Min. Soc. Amer., Washington, DC, p 291-351.

Daveler, S.A., 1998, XTOOL 7.15 user's manual: Lawrence Livermore National Laboratory, UCRL-MA-130654, 32 p.

Drummond, S.E., 1981, Boiling and mixing of hydrothermal fluids: Chemical effects on mineral precipitation: unpub. Ph.D. diss., Pennsylvania State Univ.

Fenghour, A., and Wakeman, W.A., 1998, The viscosity of carbon dioxide: J. Phys. Chem. Ref. Data, v. 27, n. 1, p. 31-44.

Fofonoff, P., and Millard, R.C., Jr., 1983, Algorithms for computation of fundamental properties of seawater: Unesco Technical Papers in Marine Sciences 44, 53 p.

Freeze, R.A., and Cherry, J.A., 1979, Groundwater: Prentice-Hall, Englewood Cliffs, NJ, 604 p.

Garrels, R.M., and Christ, C.L., 1965, Solutions, Minerals, and Equilibria: Freeman-Cooper, San Francisco, 450 p.

Gregersen, U., Johannessen, P.N., Møller, J.J., Kristensen, L., Christensen, N.P., Holloway, S., Chadwick, A., Kirby, G., Lindeberg, E., and Zweigel, P., 1998, Saline Aquifer CO_2 Storage S.A.C.S Phase Zero 1998. Internal report. GEUS (DK), BGS (UK), IKU (N). (provided courtesy of S.A.C.S.)

Helgeson, H.C., 1969, Thermodynamics of hydrothermal systems at elevated temperatures and pressures: Amer. J. Sci., v. 267, p. 729-804.

Helgeson, H.C., Delany, J.M, Nesbitt, H.W., and Bird, D.K., 1978, Summary and critique of the

thermodynamic properties of rock-forming minerals: Amer. J. Sci., v. 278-A, 229 p.

Johnson, J.W., and Lundeen, S.R., 1995, Facet: A graphical-user interface for viewing and updating the GEMBOCHS thermodynamic database: LLNL-YMP Milestone report MOL208, 28 p.

Johnson, J.W., and Lundeen, S.R., 1994a, Jewel: A graphical-user interface for generating custom GEMBOCHS thermodynamic datafiles for use with geochemical modeling software: LLNL-YMP Milestone report MOL63, 23 p.

Johnson, J.W., and Lundeen, S.R., 1994b, GEMBOCHS thermodynamic datafiles for use with the EQ3/6 software package: LLNL-YMP Milestone report MOL72, 99 p.

Johnson, J.W., and Norton, D., 1991, Critical phenomena in hydrothermal systems: State, thermodynamic, electrostatic, and transport properties of H_2O in the critical region: Amer. J. Sci., v. 291, pp. 541-648.

Johnson, J.W., Oelkers, E.H., and Helgeson, H.C., 1992, SUPCRT92: A software package for calculating the standard molal thermodynamic properties of minerals, gases, aqueous species, and reactions from 1 to 5000 bars and 0 to 1000C: Computers and Geosciences, v. 18, n. 7, p. 899-947.

Jordan, G., and Rammensee, W., 1998, Dissolution rates of calcite (1014) obtained by scanning force microscopy: Microtopography-based dissolution kinetics on surfaces with anisotropic step velocities: Geochim. Cosmochim. Acta, v. 62, n. 6., p. 941-947.

Knauss, K.G., and Copenhaver, S.A., 1995, The effect of malonate on the dissolution kinetics of albite, quartz and microcline as a function of pH at 70^{o}C: Applied Geochem., v. 10, n. 1, p. 17-33.

Knauss, K.G., and Wolery, T.J., 1989, muscovite dissolution kinetics as a function of pH and time at 70^{o}C: Geochim. Cosmochim. Acta, v. 53, p. 1493-1501.

Knauss, K.G., and Wolery, T.J., 1988, The dissolution kinetics of quartz as a function of pH and time at 70^{o}C: Geochim. Cosmochim. Acta, v. 52, p. 43-53.

Knauss, K.G., and Wolery, T.J., 1986, Dependence of albite dissolution kinetics on pH and time at 25^{o}C and 70^{o}C: Geochim. Cosmochim. Acta, v. 50, p. 2481-2497.

Lasaga, A.C., 1998, Kinetic Theory in the Earth Sciences: Princeton Univ. Press, Princeton, NJ, 811 p.

Meyer, C.A., McClintock, R.B, and Silvestri, G.J., 1993, ASME Steam Tables: Thermodynamic

and Transport Properties of Steam (comprising tables and charts for steam and water, calculated using the 1967 IFC formulation for industrial use, in conformity with the 1963 international skeleton tables, as adopted by the Sixth International Conference on the Properties of Steam), 6th ed., ASME, New York, 436 p.

Nagy, K.L., 1995, Dissolution and precipitation kinetics of sheet silicates: in White, A.F., and Brantley, S.L. (Eds.), Chemical Weathering Rates of Silicate Minerals: Rev. Min., v. 31, Min. Soc. Amer., Washington, DC, p 173-233.

Nitao, J.J., 1998a, Reference manual for the NUFT flow and transport code, version 2.0: Lawrence Livermore National Laboratory, UCRL-MA-130651, 55 p.

Nitao, J.J., 1998b, User's manual for the USNT module of the NUFT Code, Version 2.0 (NP-Phase, NC-component, Thermal): Lawrence Livermore National Laboratory, UCRL-MA-130653, 76 p.

Nitao, J.J., 2001, User's manual for the TRANS module of the NUFT Code (in prep.).

Parker, J.C., Lenhard, R.J., and Kuppusamy, T., 1987, A parametric model for constitutive properties governing multiphase flow in porous media: Water Resources Research, v. 23, n. 4, p. 618-624.

Pokrovsky, O.S., and Schott, J., 1999, Processes at the magnesium-bearing carbonates solution interface. II. Kinetics and mechanism of magnesite dissolution: Geochim. Cosmochim. Acta, v. 63, n. 6, p. 881-897.

Renders, P.J.N., Gammons, C.H., and Barnes, H.L., 1995, Precipitation and dissolution rate constants for cristobalite from 150 to 300°C: Geochim. Cosmochim. Acta, v. 59, n. 1, p. 77-85.

Robie, R.A., Hemingway, B.S., and Fisher, J.R., 1978, Thermodynamic properties of minerals and related substances at 298.15 K and 1 bar (10^5 Pascals) pressure and at higher temperatures: U.S.G.S. Bull. 1452, 456 p.

SACS, 2000, Final Technical Report "SACS" – Saline Aquifer CO_2 Storage, 34 p. (available on the SACS web site: http://www.ieagreen.org.uk/sacshome.htm)

Scheidegger, A.E., 1974, The Physics of Flow through Porous Media (3rd ed.): Univ. Toronto Press, Toronto, 353 p.

Shock, E.L., 1998, An updated and augmented version (slop98.dat) of the original SUPCRT92 database (sprons92.dat) is available on the Dr. Shock's website: http://zonvark.wustl.edu/geopig/

Shock, E.L., Oelkers, E.H., Johnson, J.W., Sverjensky, D.A., and Helgeson, H.C., 1992, Calculation of the thermodynamic properties of aqueous species at high pressures and temperatures: Effective electrostatic radii, dissociation constants, and standard partial molal properties to 1000C and 5 kb: Journal of the Chemical Society (London) Faraday Transactions, v. 88, n. 6, p. 803-826.

Span, R., and Wagner, W., 1996, A new equation of state for carbon dioxide covering the fluid region from the triple-point temperature to 1100 K at pressures up to 800 MPa: J. Phys. Chem. Ref. Data, v. 25, n. 6, p. 1509-1596.

Steefel, C.I., 2001, CRUNCH: Software for multicomponent reactive transport (in prep.).

Stillings, L.L., Drever, J.I., Brantley, R.L., Sun, Y., and Oxburgh, R., 1996, Rates of feldspar dissolution at pH 3-7 with 0-8 mM oxalic acid: Chem. Geol., v. 132, p. 79-89.

Tanger, J.C. IV, and Helgeson, H.C., 1988, Calculation of the thermodynamic and transport properties of aqueous species at high pressures and temperatures: Revised equations of state for the standard partial molal properties of ions and electrolytes: Amer. J. Sci., v. 288, n. 1, p. 19-98.

Tester, J.W., Worley, W.G., Robinson, B.A., Grigsby, C.O., and Feerer, J.R., 1994, Correlating quartz dissolution rates in pure water from 25 to 625^{o}C: Geochim. Cosmochim. Acta, v. 58, n. 11, p. 2407-2420.

Wolery, T.J., 1992, EQ3/6, A software package for geochemical modeling of aqueous systems: Package overview and installation guide (Version 7.0): Lawrence Livermore National Laboratory, UCRL-MA-110662 PT 1, 66 p.

Table 1: Lithologic state conditions and hydrologic properties at Sleipner

parameter	**Utsira Formation**[1]	**saline aquifer**[2]	**shale cap rock**[2,3]	**intra-aquifer shales (CSH)**[2,3]	**intra-aquifer shales (DSH)**[2,3]
T (^{o}C)	37	37	37	37	37
P (bars)	80-110	90-110	87.5-90	---	---
poros. (%)	35-40	35	5	5	5
perm. (m^2)	(1-8)(10^{-12})	3(10^{-12})	3(10^{-18})	3(10^{-15})	3(10^{-18})
thickness (m)	150-250	200	25	3	3

[1] from Gregersen et al. (1998)
[2] adopted in this study
[3] Sleipner-specific data are unavailable (see text)

Table 2: Lithologic mineralogies at Sleipner; abundances given in volume percent.

mineral	**Miocene sand**[1]	**saline aquifer**[2]	**shale**[2,3]
quartz	79	80	35
K-feldspar	6	10	5
Plagioclase	3	5	---
“Mica”	5	---	---
calcite	5	---	---
“Clay”	1	---	---
muscovite	---	3	50
phlogopite	---	2	---
Mg-chlorite	---	---	10

[1] provided courtesy of Tore Torp (Statoil) and Niels Springer (GEUS) as a proxy for an analysis from the Utsira Formation (pers. comm.)
[2] adopted in the present study (see text)
[3] Sleipner-specific data are unavailable (see text)

Table 3: Comparison of fluid compositions reported for seawater, the concentrations in molality unless otherwise noted)

component	seawater[a]	Oseberg[b]	this study
Sodium	0.48	0.4520	Oseberg
Potassium	0.010	0.0053	Oseberg
Calcium	0.010	0.0106	0.00742[c]
Magnesium	0.054	0.0259	0.01813[c]
Strontium	unreported	$1.14(10^{-4})$	0[d]
Barium	unreported	$3.64(10^{-6})$	0[d]
Aluminum	unreported	unreported	$1.3(10^{-8})$[e]
Silica	unreported	unreported	$1.664(10^{-4})$[f]
Iron [total]	unreported	$3.58(10^{-5})$	0[g]
Chloride	0.56	0.5213	Oseberg
Bicarbonate	0.0024	0.0116	0.00232[h]
Carbonate	$2.7(10^{-4})$	unreported	---[i]
Sulphate	0.028	undetected	Oseberg (0)
Oxygen [O_2(aq)] (ppb)	unreported	5	0[j]
pH	8.15	7.1	7.0-7.2[k]

[a] average surface seawater at 25°C (Garrels and Christ, 1965)
[b] from Gregersen et al. (1998), who report concentrations in g/L; this analysis is from the Utsira formation at Oseberg, about 200 km north of Sleipner
[c] 70% of Oseberg value; reduced to obtain undersaturation with respect to calcite and magnesite (see text)
[d] trace concentrations removed
[e] between K-feld+Mucovite and kaolinite+quartz equilibrium (37°C, 100 bars)
[f] quartz equilibrium (37°C, 100 bars)
[g] removed because ferrous/ferric partitioning cannot be constrained (see footnote j)
[h] 20% of Oseberg value (roughly equivalent to average seawater); reduced to obtain undersaturation with respect to calcite and magnesite (see text)
[i] in this study, "bicarbonate" concentration combines both bicarbonate and carbonate contributions
[j] removed because the Oseberg value is unrealistically high (see text); as a result, the *in situ* oxidation state cannot be determined
[k] range encompasses background pH evolution within both the saline aquifer and all shales) over the 20-year simulation

Table 4: Summary of adopted kinetic data for primary (boldface) and observed (precipitated) secondary minerals.

mineral	P_r-T_r diss/pptn rate constant[a,b] (mol m^{-2} s^{-1})	activation energy[a] (kJ mol^{-1})	reactive specific surface area[c] (m^2 m^{-3})$_{mineral}$	surface area scaling factor[d]
quartz	$1.035(10^{-14})$[e]	87.7[e]	$5.741(10^4)$	2.39
K-feldspar	$1.778(10^{-10})$[f]	51.7[f]	$1.113(10^5)$	4.64
plag-Ab80	$5.623(10^{-13})$[f]	80.3[f]	$8.752(10^4)$	3.65[iq]
muscovite	$1.000(10^{-13})$[g]	22.0[g]	$1.246(10^6)$	51.90
phlogopite	$4.000(10^{-13})$[g]	29.0[g]	$1.246(10^6)$	51.90[n]
Mg-chlorite[p]	$3.000(10^{-13})$[g]	88.0[g]	$1.246(10^6)$	51.90[n]
magnesite	$1.000(10^{-9})$[h]	62.8[i]	---	---
dawsonite	$1.000(10^{-7})$[il]	62.8[i]	---	---
calcite	$1.500(10^{-6})$[j]	62.8[i]	---	---
cristobalite	$3.450(10^{-13})$[k]	62.8[i]	---	---
chalcedony	$3.450(10^{-13})$[im]	62.8[i]	---	---
kaolinite	$4.000(10^{-13})$[g]	29.0[g]	---	---
talc	$1.000(10^{-12})$[g]	42.0[g]	---	---
paragonite	$1.000(10^{-13})$[in]	22.0[in]	---	---
pyrophyllite	$4.000(10^{-13})$[io]	29.0[io]	---	---
gibbsite	$3.000(10^{-13})$[g]	62.8[i]	---	---

[a] adopted data are those for the relevant acidic conditions (pH 4-5.5)
[b] dissolution and precipitation rate constants are taken to be of equal magnitude
[c] specific surface areas (SSA) are those of the relevant grain-size-fraction spheres multiplied by the surface area scaling factor; *reactive* SSA are SSA multiplied by the fraction of SSA presumed available for chemical reactions; reactive SSA for each mineral is equivalent in the aquifer sand and in shales (see text)
[d] scales spherical SSA by the factor of increase observed for 100-micron mineral grains whose SSA has been measured using BET methods (see text)
[e] Tester et al. (1994)
[f] Blum and Stillings (1995)
[g] Nagy (1995)
[h] Pokrovsky and Schott (1999)
[i] estimated in the present study
[j] Jordan and Rammensee (1998)
[k] Renders et al. (1995)
[l] estimated as intermediate to calcite and magnesite
[m] presumed equivalent to cristobalite
[n] presumed equivalent to muscovite
[o] presumed equivalent to kaolinite
[p] clinochlore-14A
[q] based on observed scaling factors for albite and anorthite

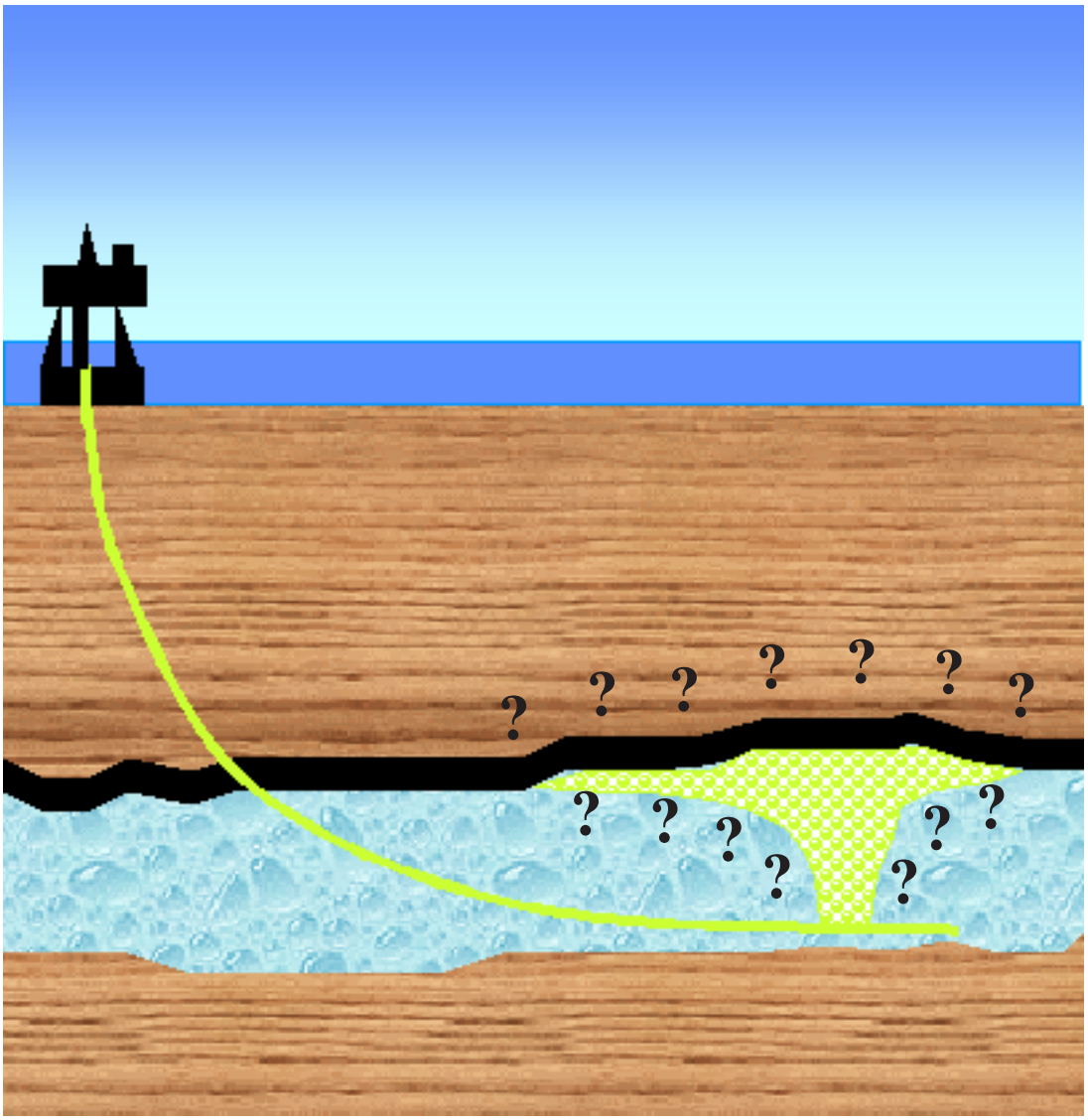

Figure 1: Schematic illustration of CO_2 injection into a confined saline aquifer at Statoil's North-Sea Sleipner facility. Question marks signify the current ring of uncertainty that surrounds the ultimate fate of injected CO_2 waste streams.

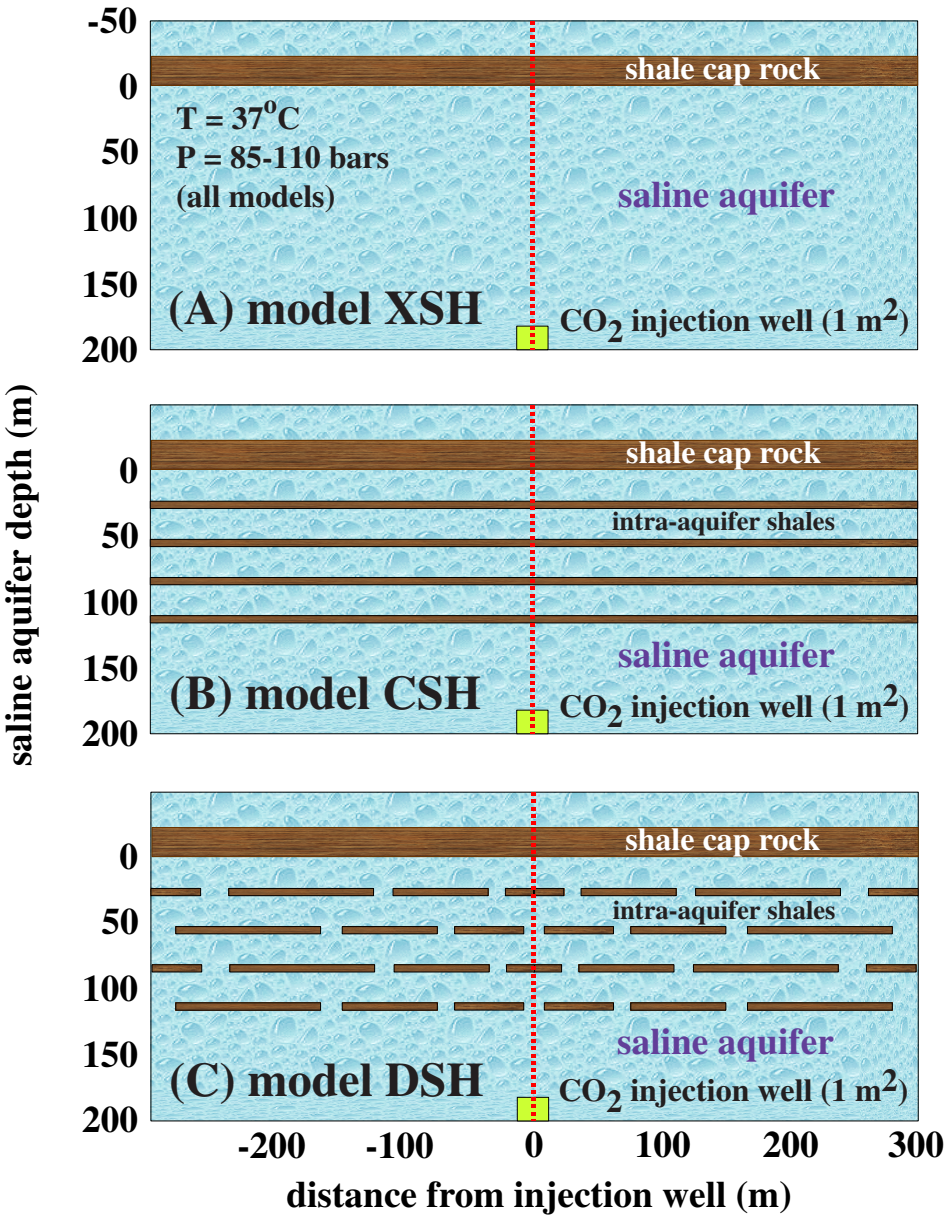

Figure 2: Schematic depiction of the near-field spatial domain adopted for reactive transport simulations of CO_2 injection at Sleipner in models XSH, CSH, and DSH. The dotted red line marks the left-hand side of the actual simulation regions, which are then reflected across this symmetry plane to obtain the composite 250x1x600 m (x-y-z) domains.

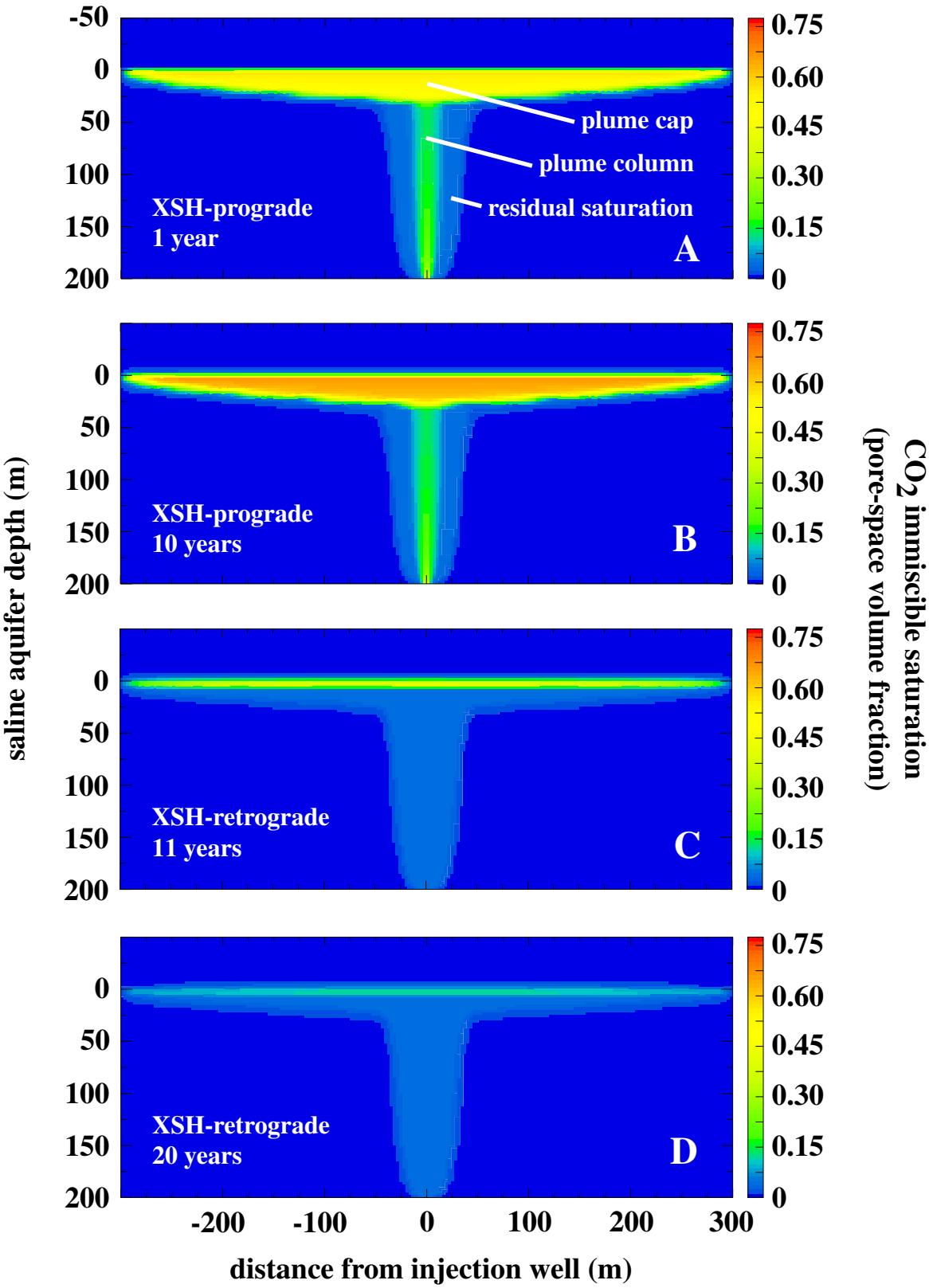

Figure 3: Evolution of CO_2 immiscible saturation in model XSH during prograde (1 and 10 years) and retrograde (11 and 20 years) sequestration.

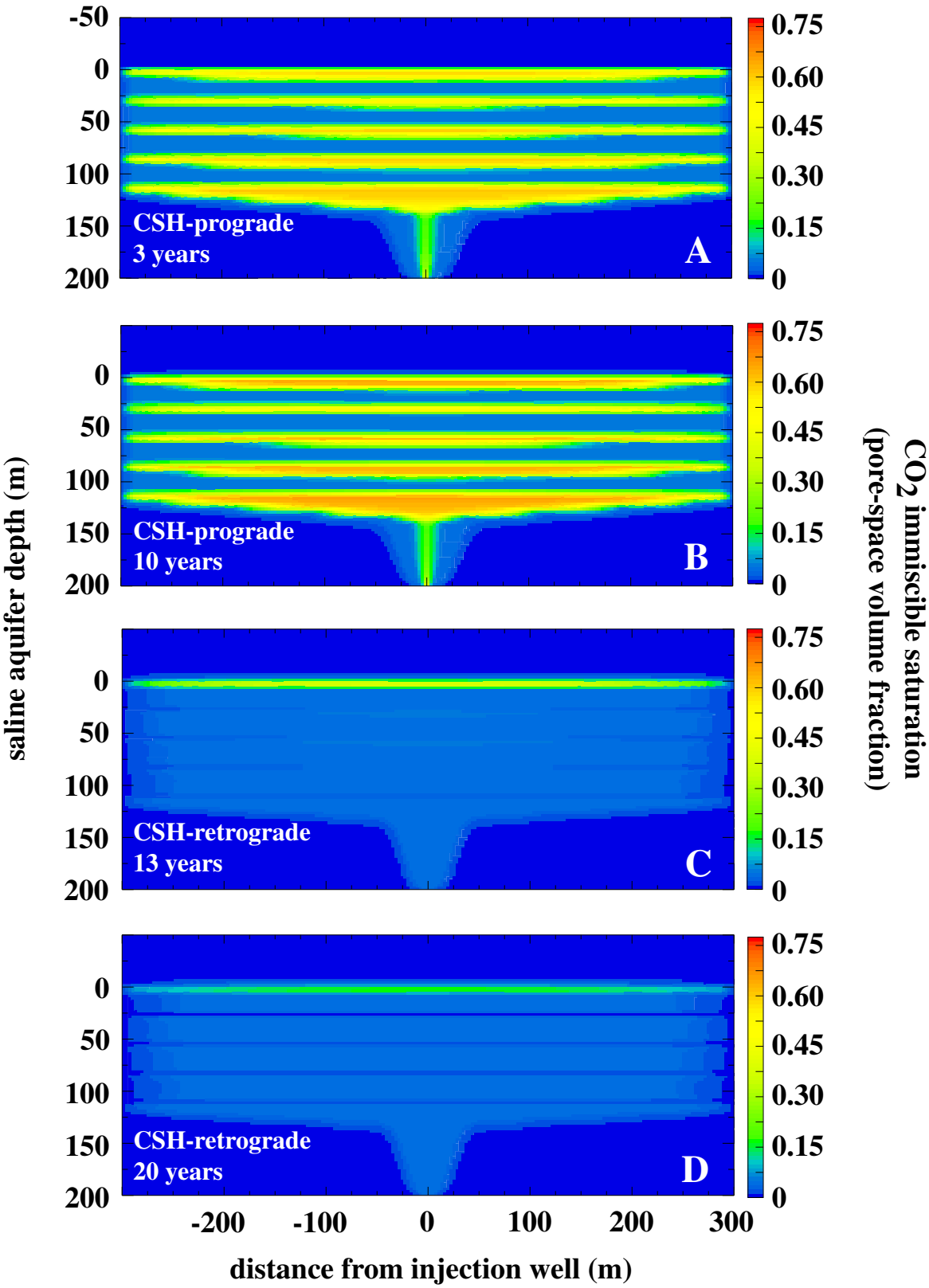

Figure 4: Evolution of CO_2 immiscible saturation in model CSH during prograde (3 and 10 years) and retrograde (13 and 20 years) sequestration.

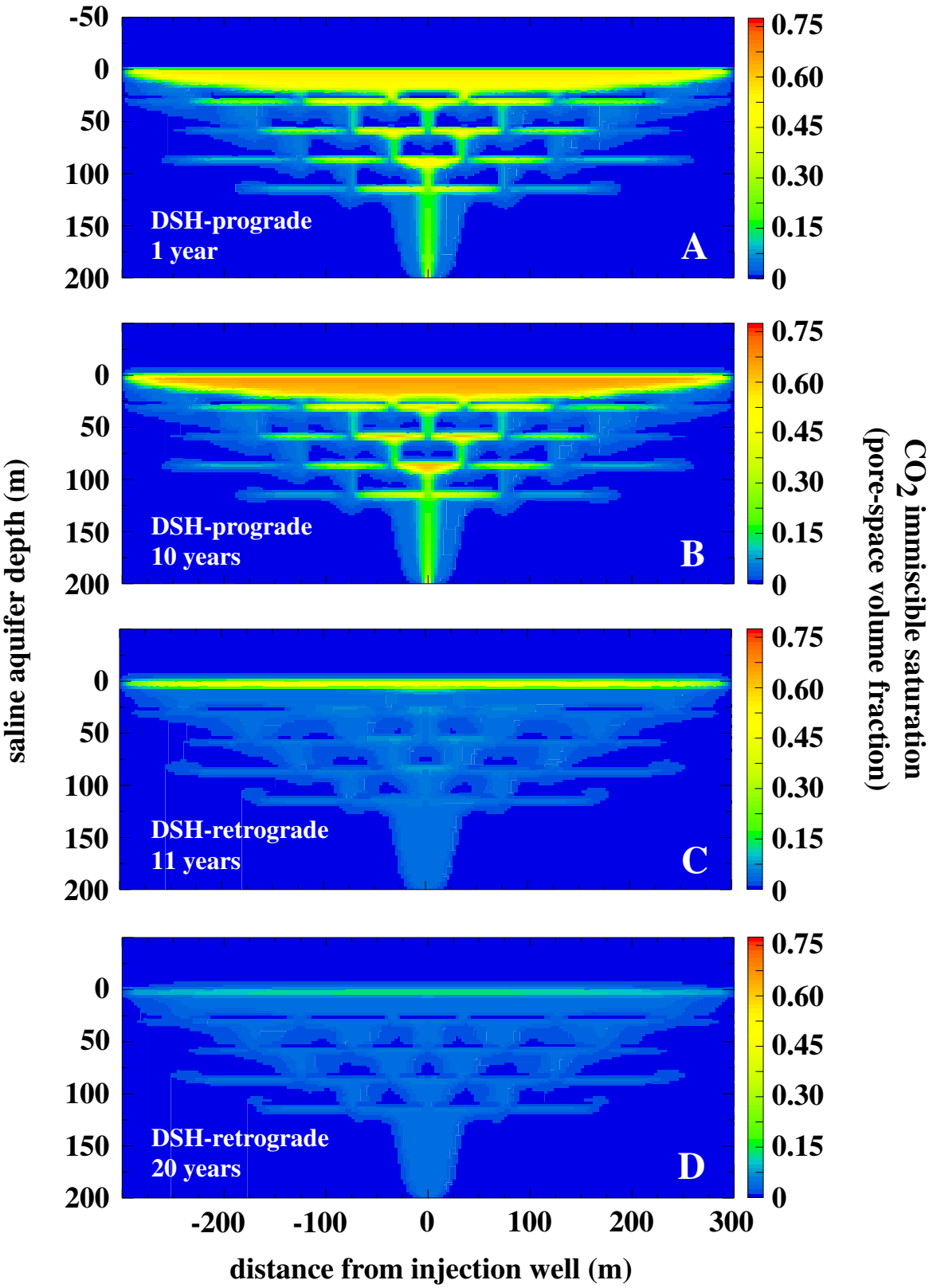

Figure 5: Evolution of CO_2 immiscible saturation in model DSH during prograde (1 and 10 years) and retrograde (11 and 20 years) sequestration.

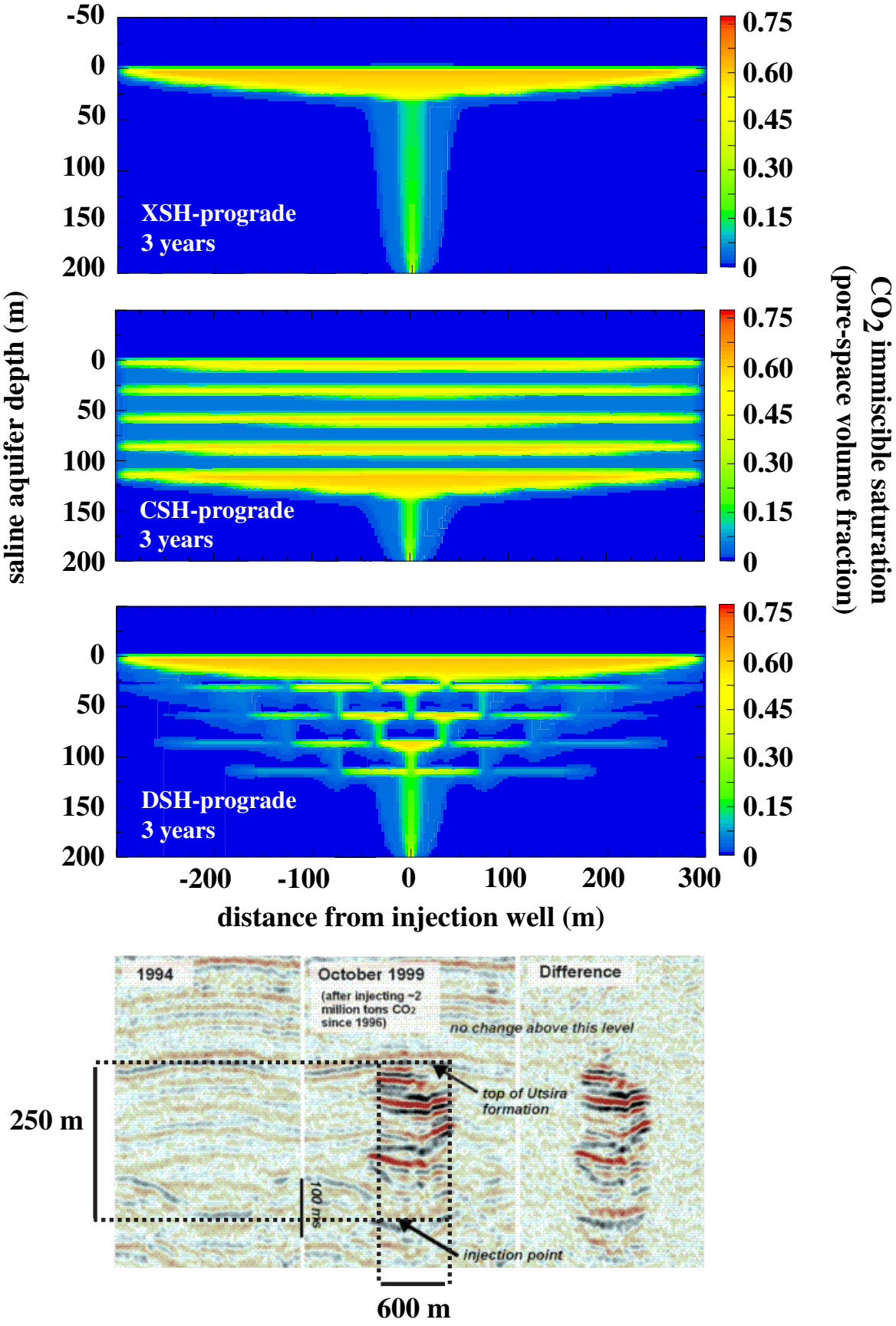

Figure 6: CO_2 immiscible saturation in models XSH, DSH, and CSH after 3 years of injection juxtaposed above a seismic profile of CO_2 accumulations at Sleipner after the same time span (central panel of the bottom figure). Breakout scale bars that delineate the simulation domains have been added to the original seismic image, which appears on the cover of the IEA-GHG R&D Programme Annual Report 1999 and is avaiable on their web site (http://www.ieagreen.org.uk).

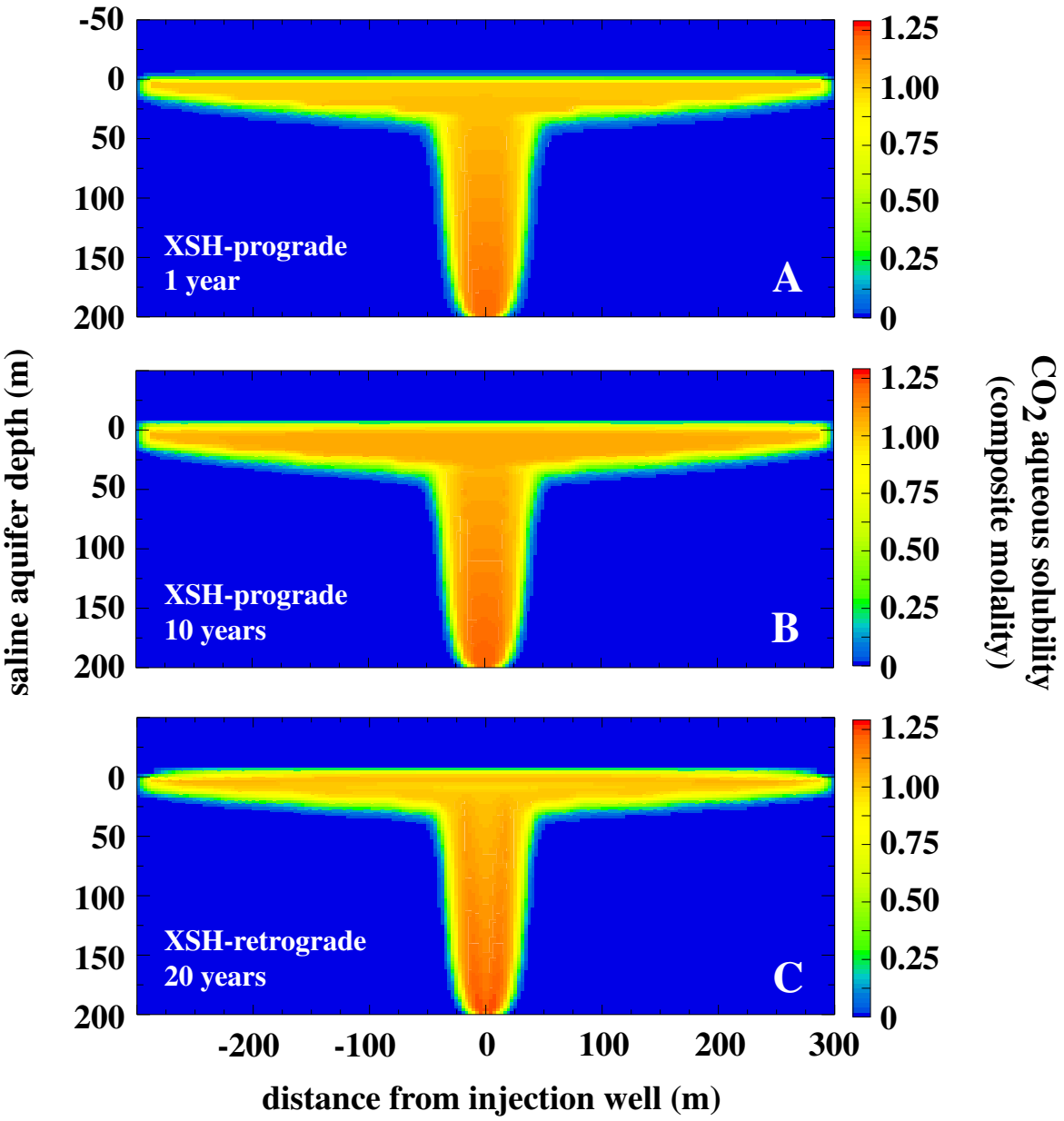

Figure 7: Evolution of CO_2 aqueous solubility (composite molality of all carbon-bearing aqueous solutes) in model XSH during prograde (1 and 10 years) and retrograde (20 years) sequestration.

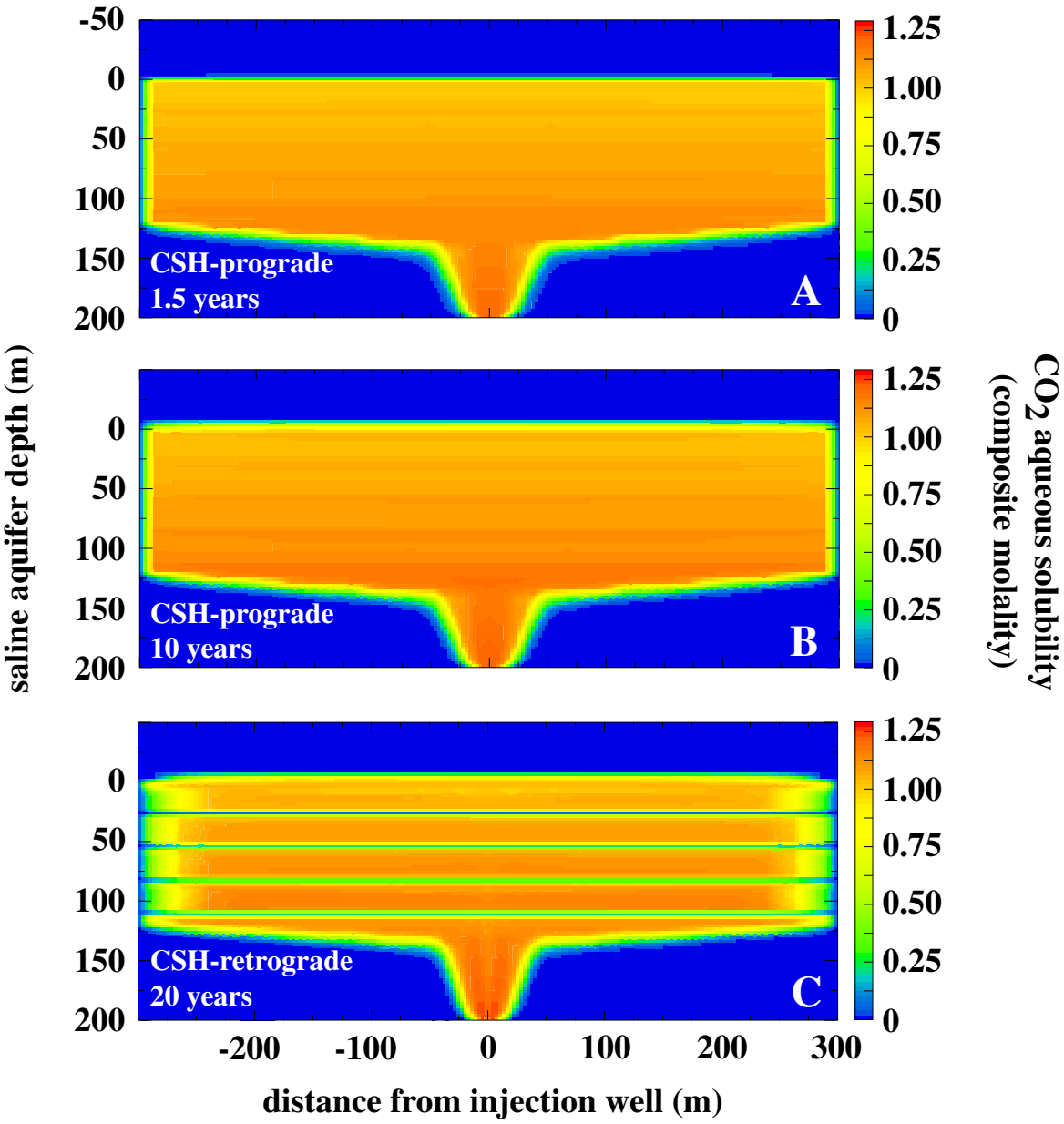

Figure 8: Evolution of CO_2 aqueous solubility (composite molality of all carbon-bearing aqueous solutes) in model CSH during prograde (1.5 and 10 years) and retrograde (20 years) sequestration.

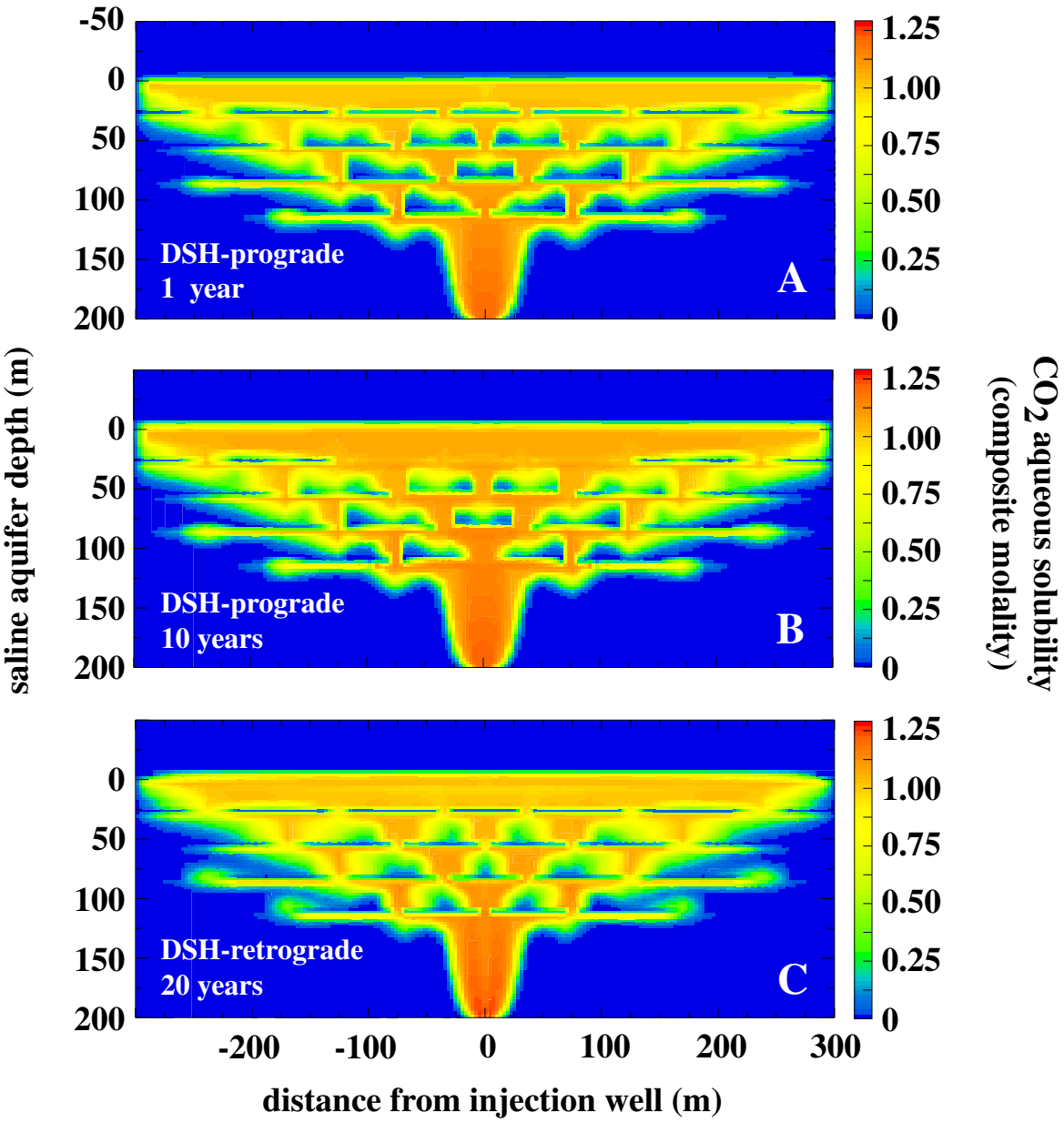

Figure 9: Evolution of CO_2 aqueous solubility (composite molality of all carbon-bearing aqueous solutes) in model DSH during prograde (1 and 10 years) and retrograde (20 years) sequestration.

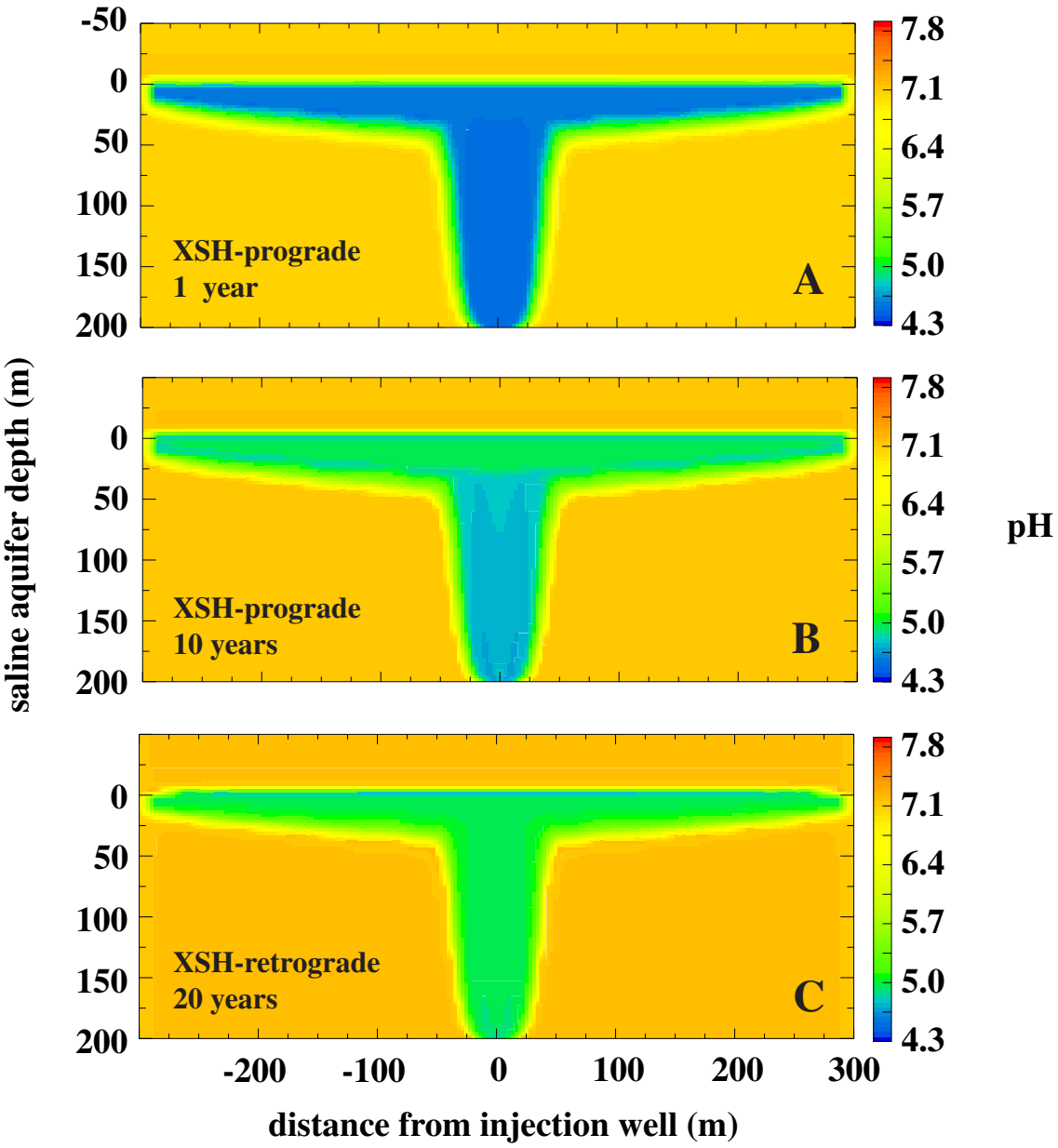

Figure 10: Evolution of pH in model XSH during prograde (1 and 10 years) and retrograde (20 years) sequestration.

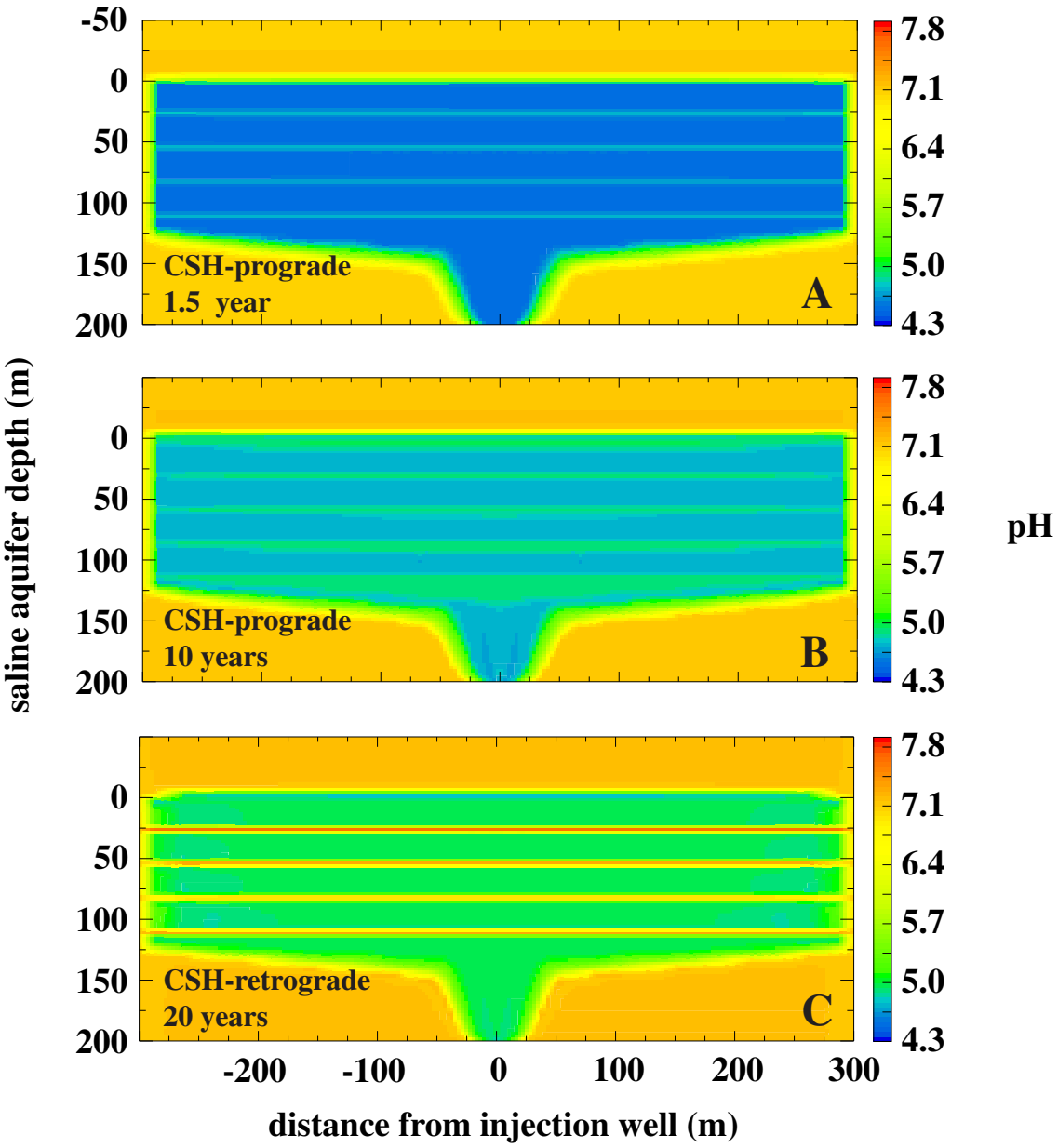

Figure 11: Evolution of pH in model CSH during prograde (1.5 and 10 years) and retrograde (20 years) sequestration.

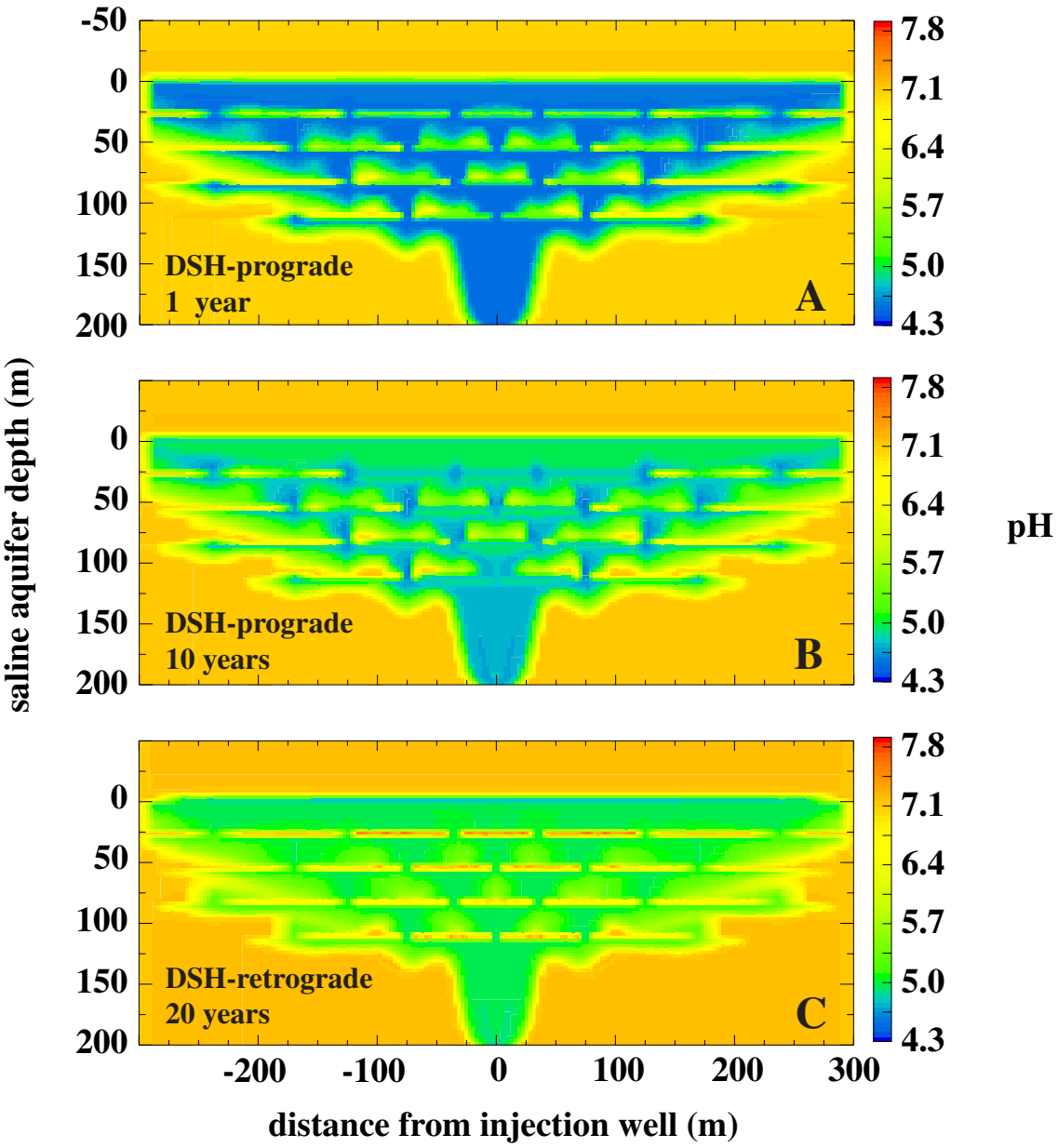

Figure 12: Evolution of pH in model DSH during prograde (1 and 10 years) and retrograde (20 years) sequestration.

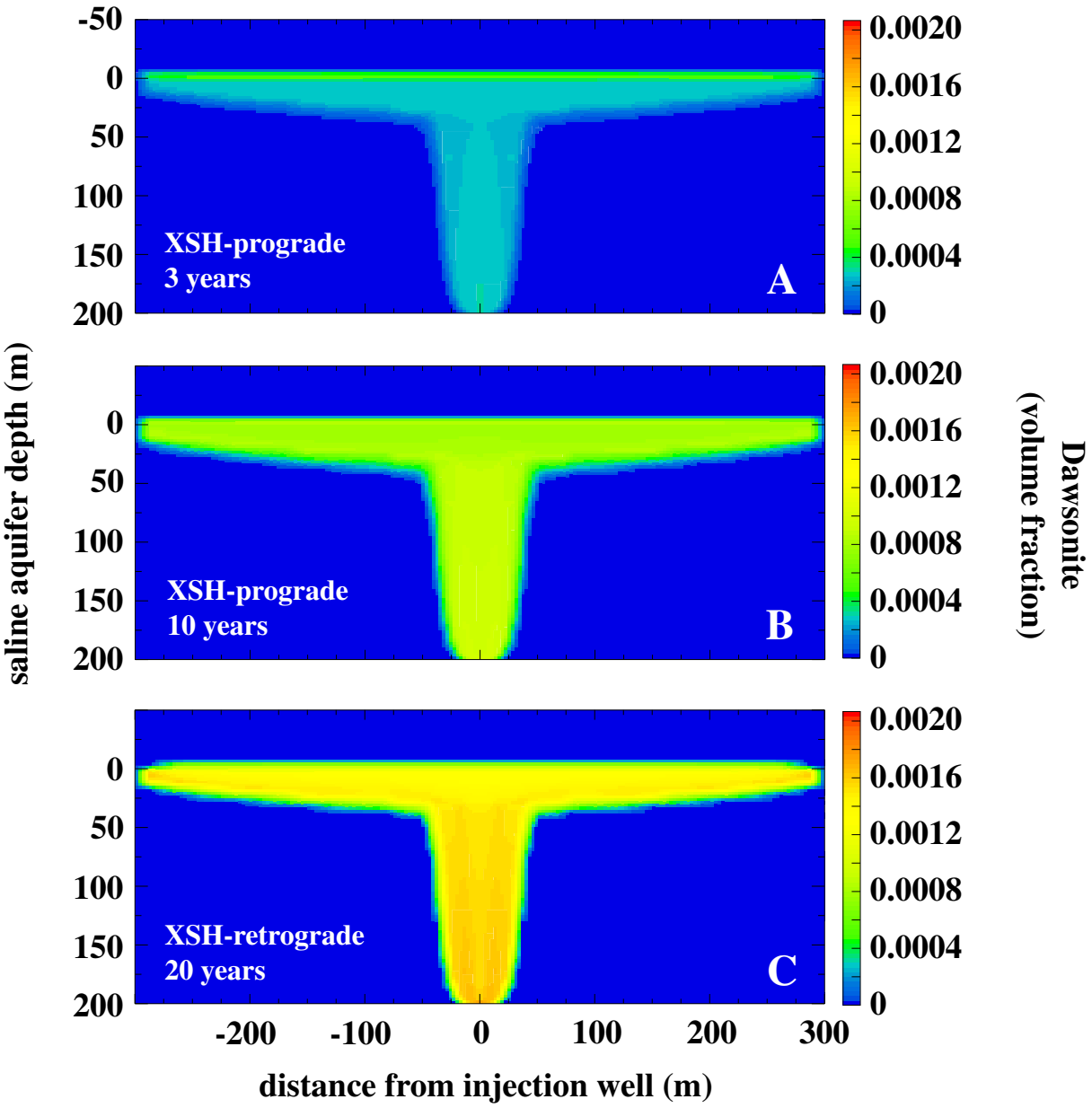

Figure 13: Evolution of Dawsonite [$NaAlCO_3(OH)_2$] precipitation in model XSH during prograde (3 and 10 years) and retrograde (20 years) sequestration.

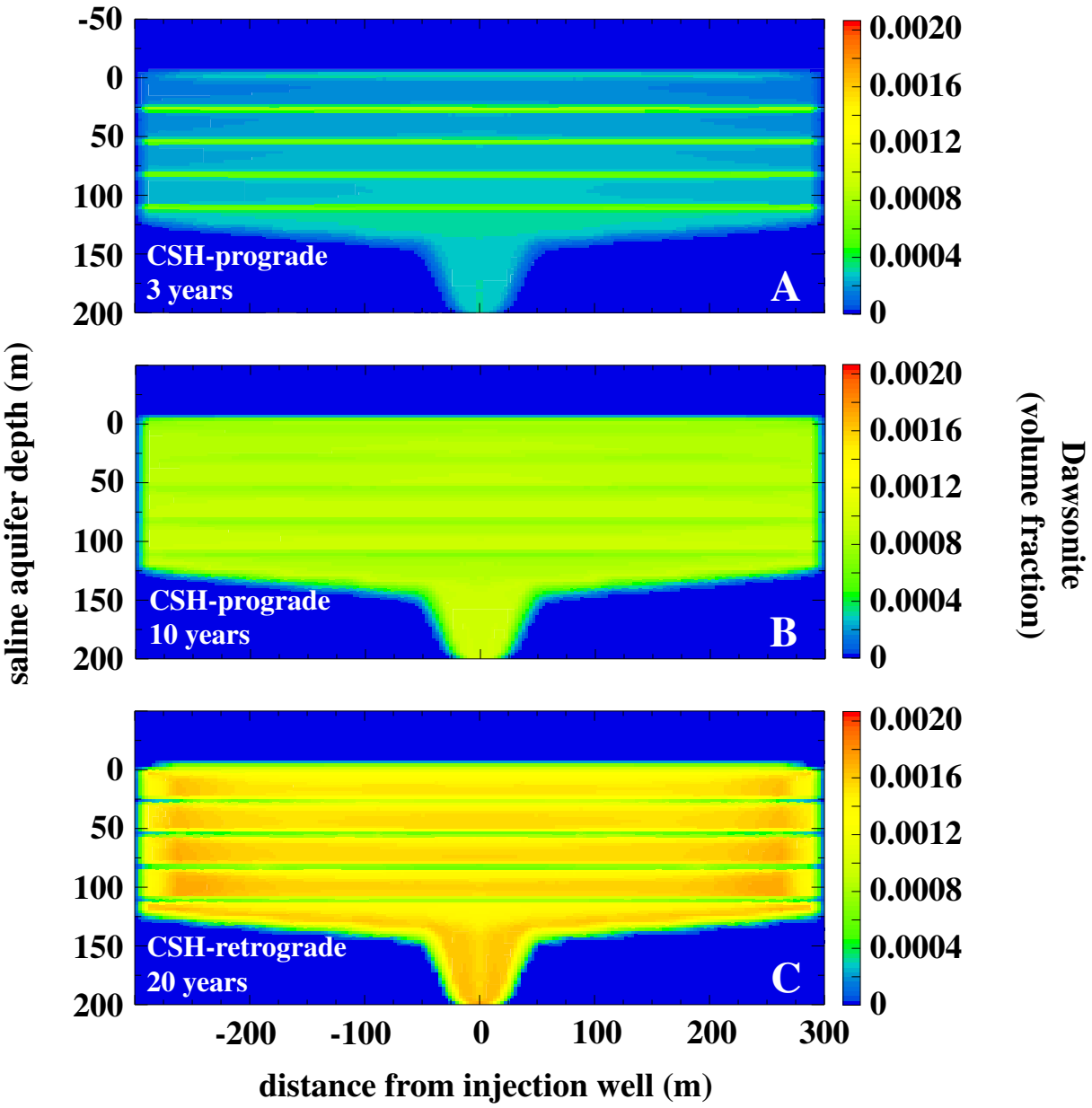

Figure 14: Evolution of Dawsonite [$NaAlCO_3(OH)_2$] precipitation in model CSH during prograde (3 and 10 years) and retrograde (20 years) sequestration.

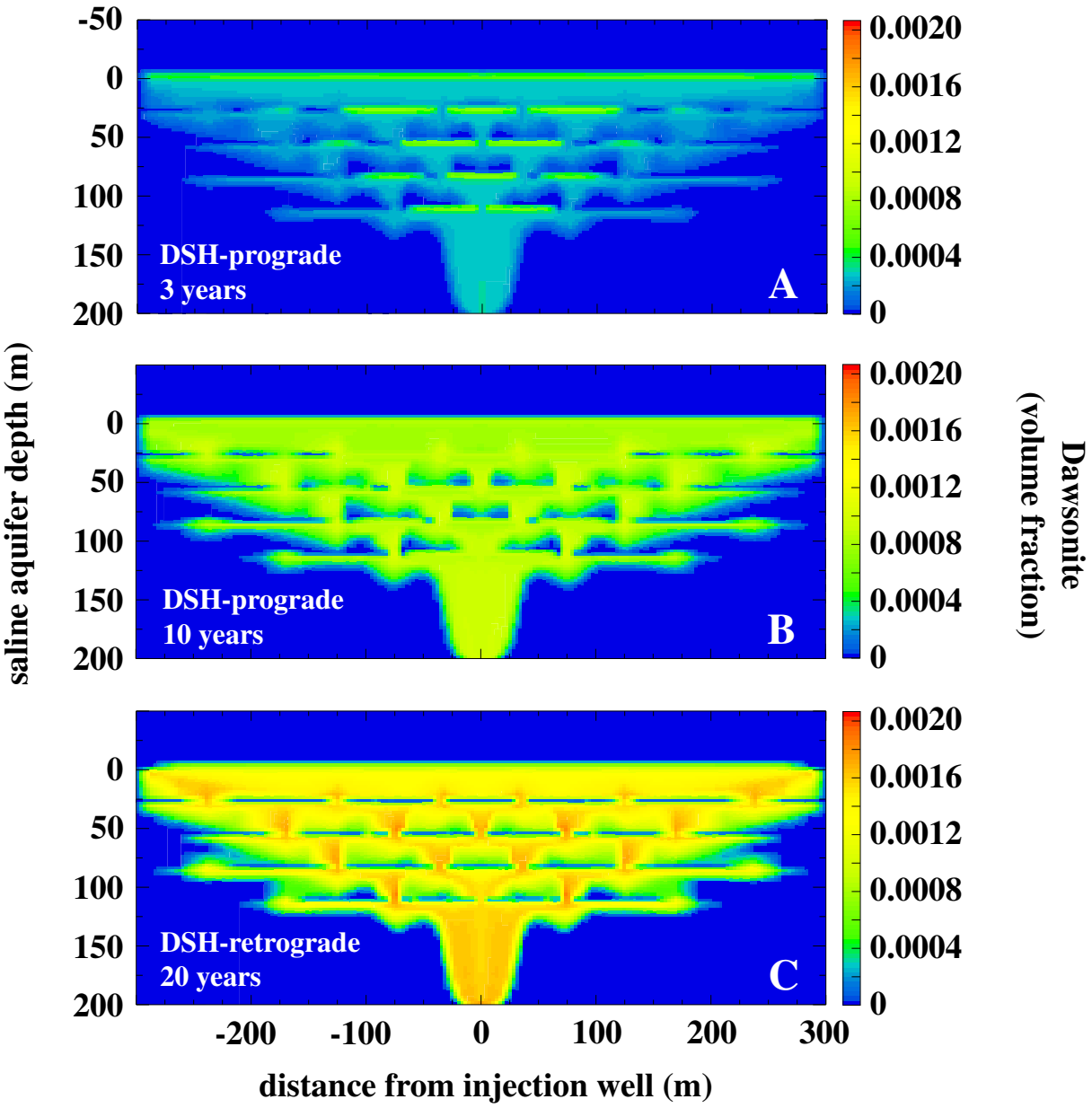

Figure 15: Evolution of Dawsonite [$NaAlCO_3(OH)_2$] precipitation in model DSH during prograde (3 and 10 years) and retrograde (20 years) sequestration.

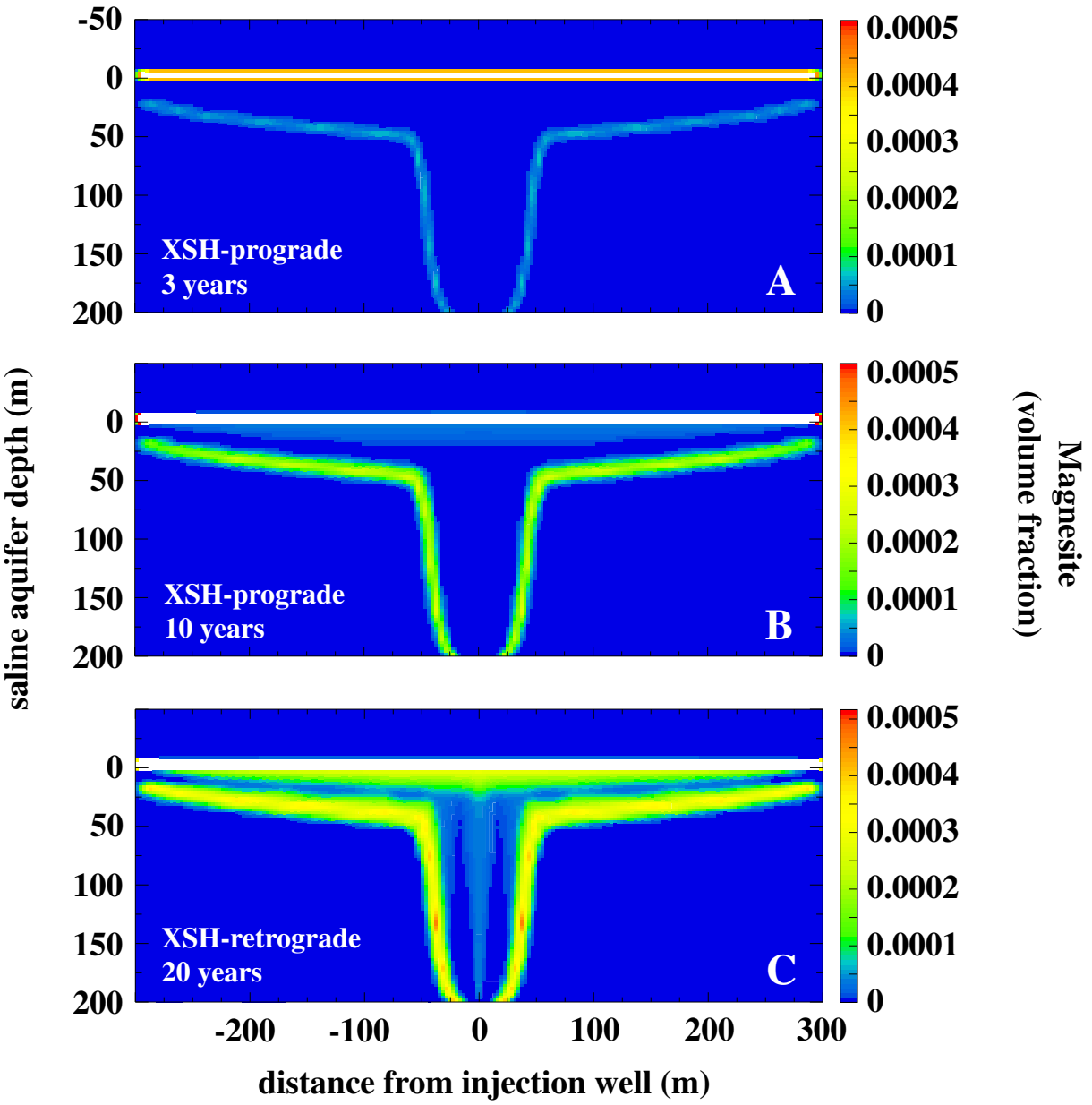

Figure 16: Evolution of Magnesite [$MgCO_3$] precipitation within the saline aquifer of model XSH during prograde (3 and 10 years) and retrograde (20 years) sequestration.

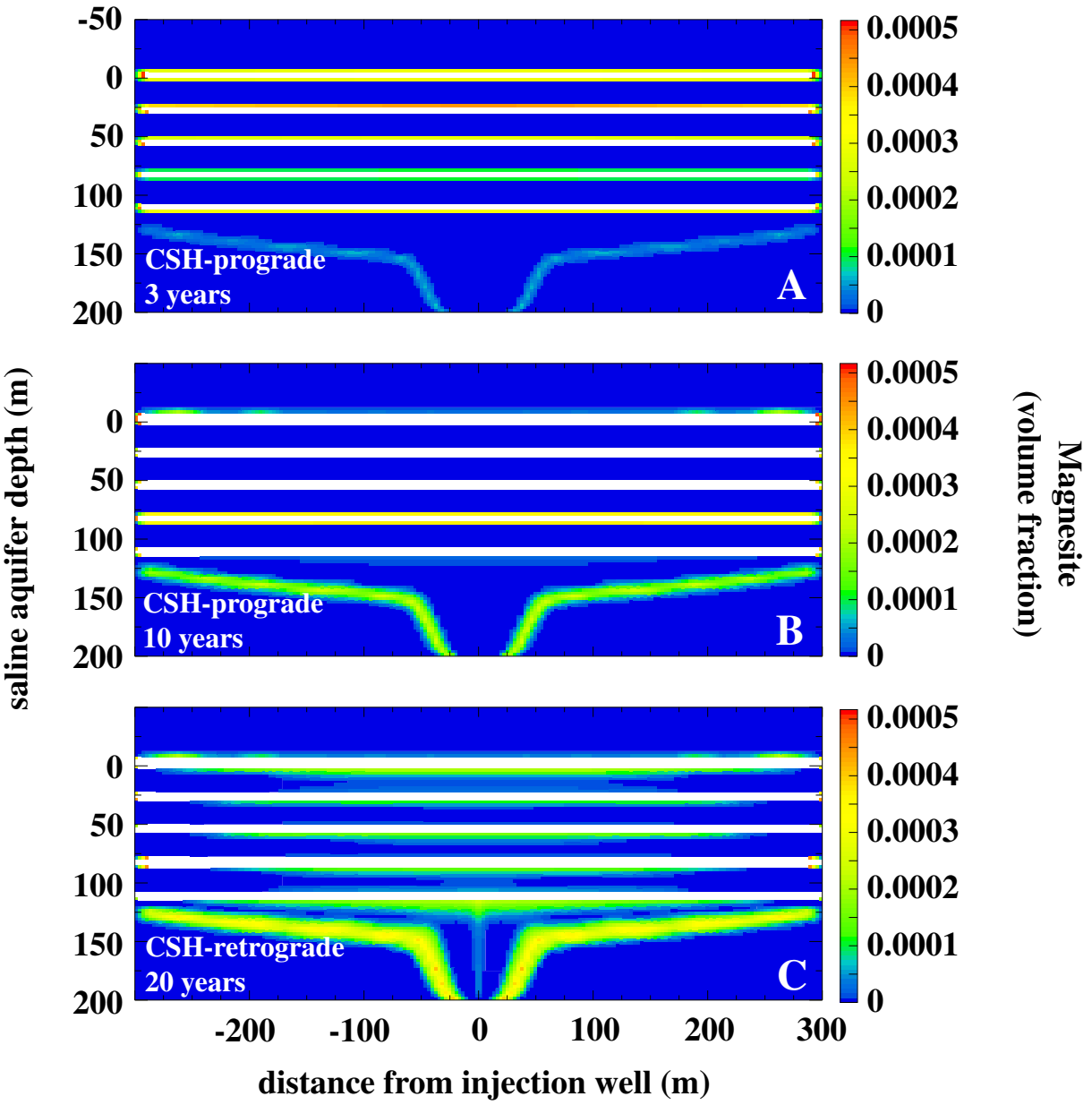

Figure 17: Evolution of Magnesite [$MgCO_3$] precipitation within the saline aquifer of model CSH during prograde (3 and 10 years) and retrograde (20 years) sequestration.

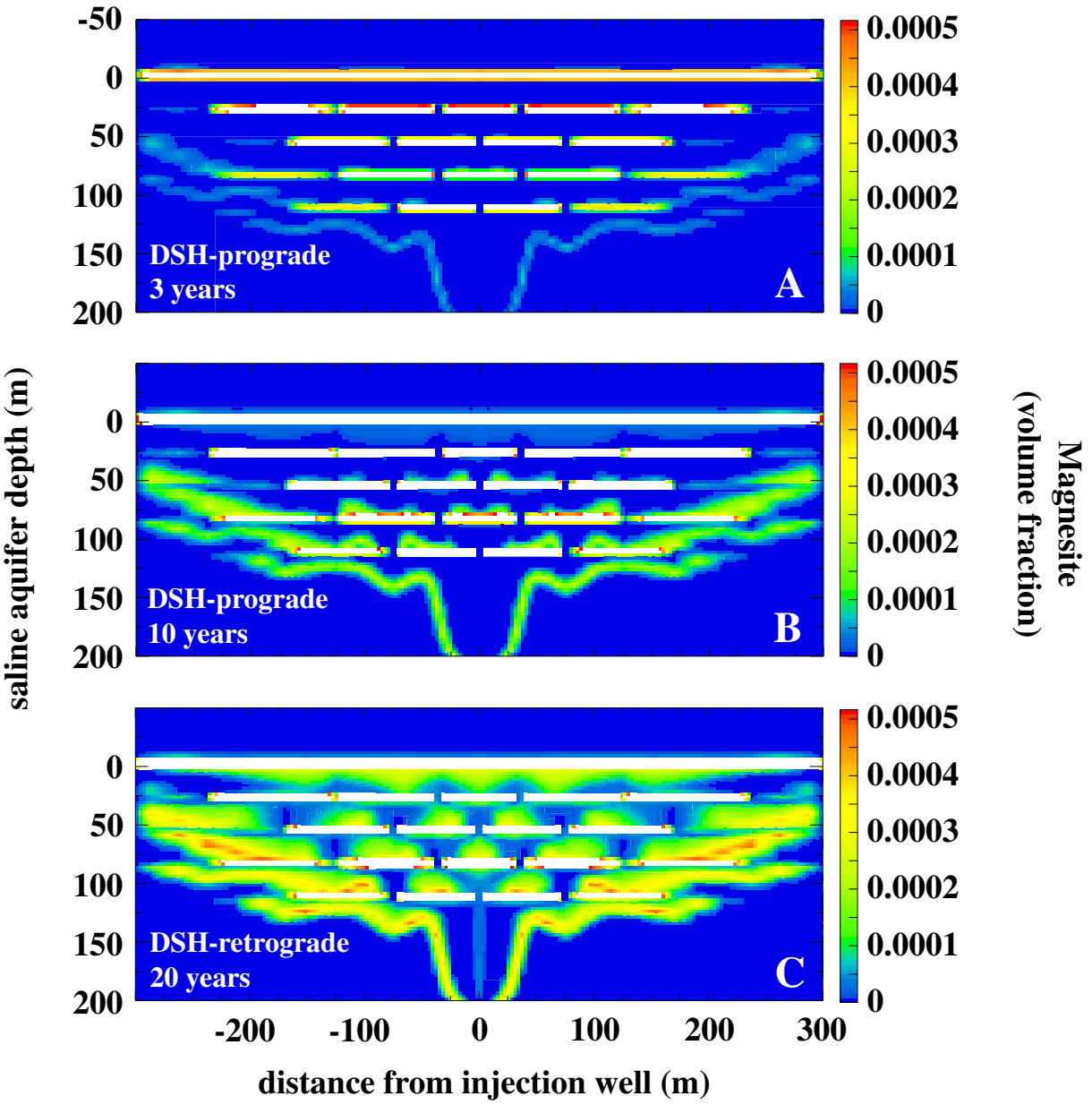

Figure 18: Evolution of Magnesite [$MgCO_3$] precipitation within the saline aquifer of model DSH during prograde (3 and 10 years) and retrograde (20 years) sequestration.

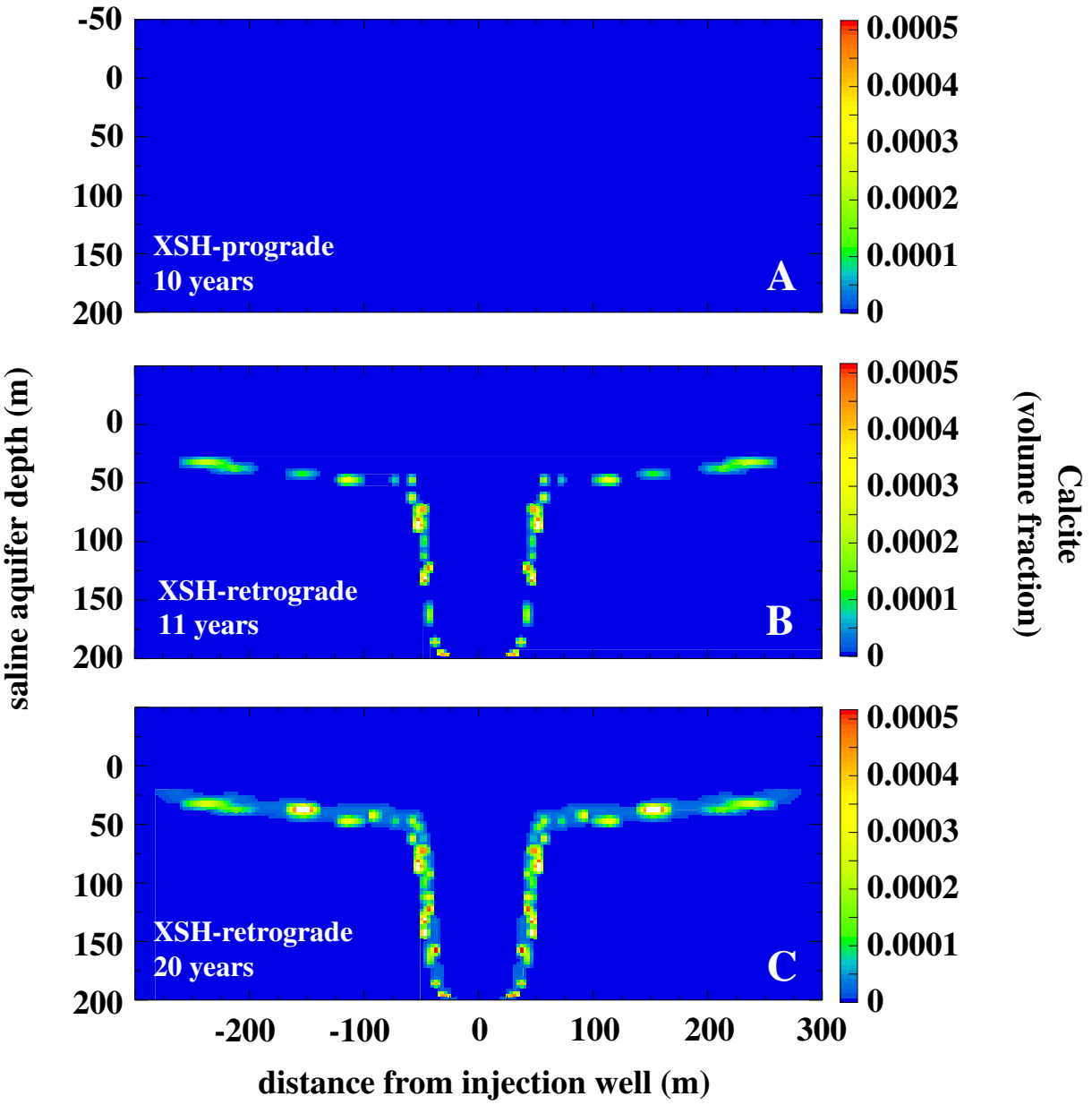

Figure 19: Evolution of Calcite [$CaCO_3$] precipitation within the saline aquifer of model XSH during prograde (10 years, no precipitation) and retrograde (11 and 20 years) sequestration.

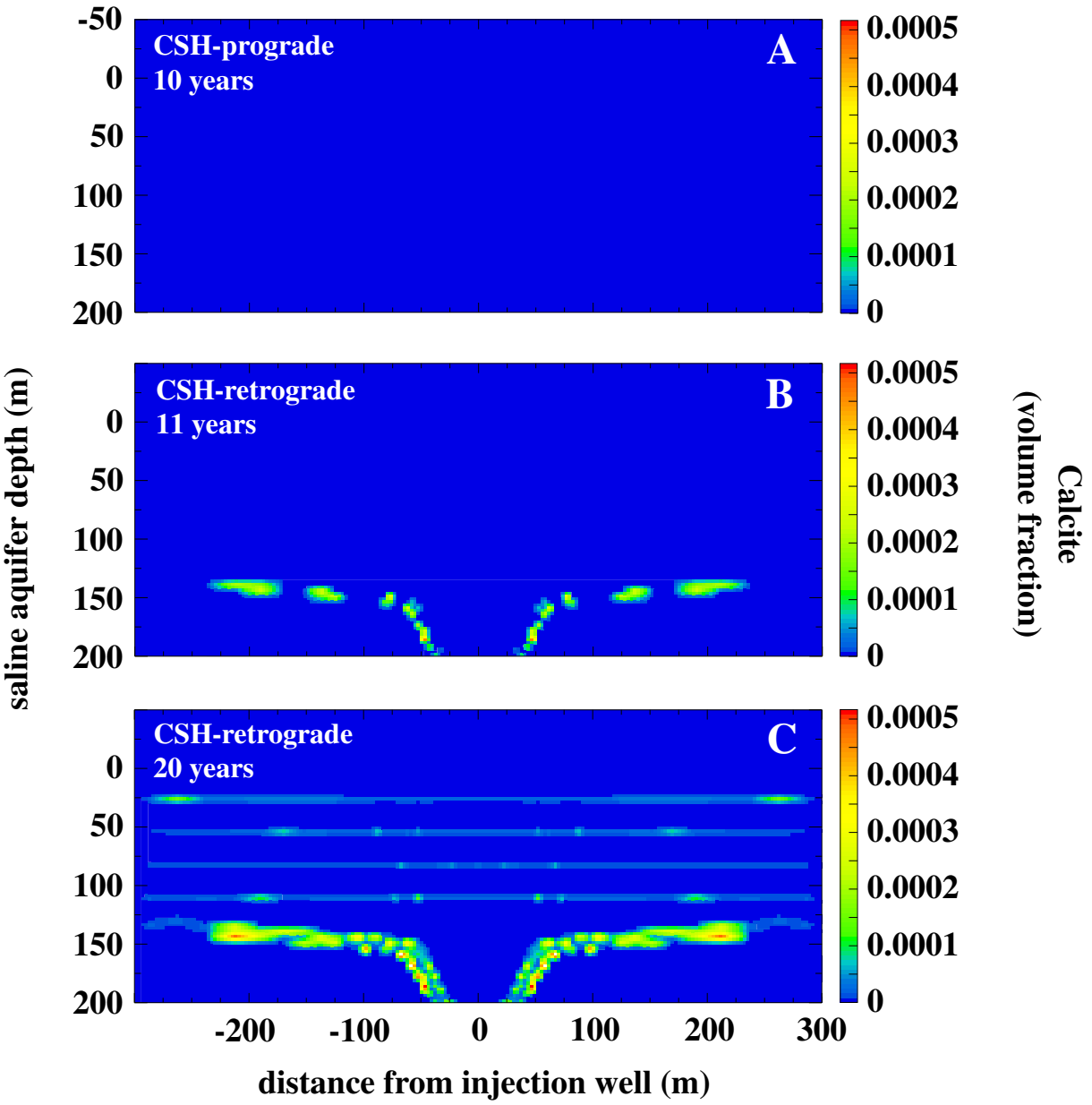

Figure 20: Evolution of Calcite [$CaCO_3$] precipitation within the saline aquifer and intra-aquifer shales of model CSH during prograde (10 years, no precipitation) and retrograde (11 and 20 years) sequestration.

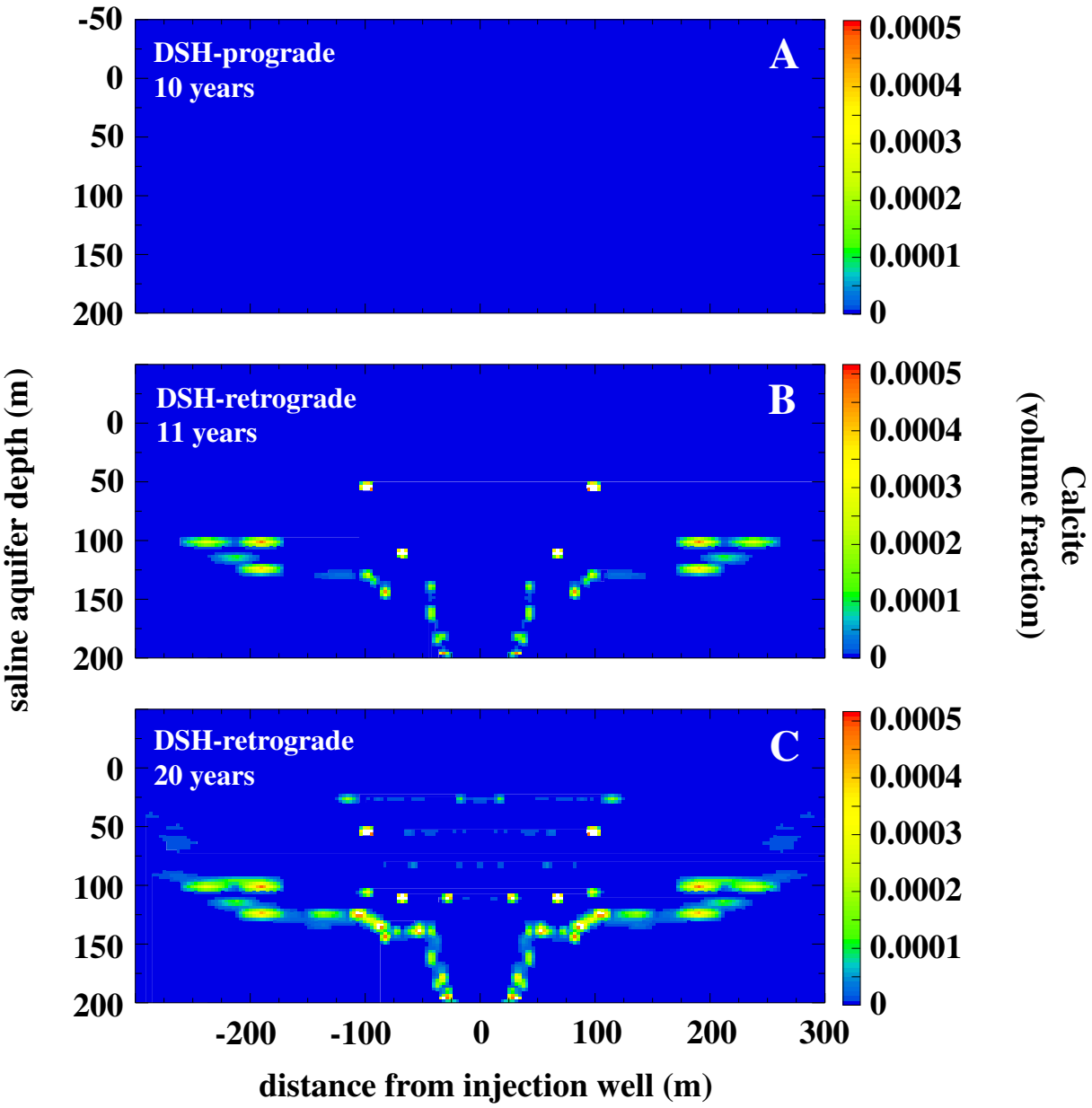

Figure 21: Evolution of Calcite [$CaCO_3$] precipitation within the saline aquifer and intra-aquifer shales of model DSH during prograde (10 years, no precipitation) and retrograde (11 and 20 years) sequestration.

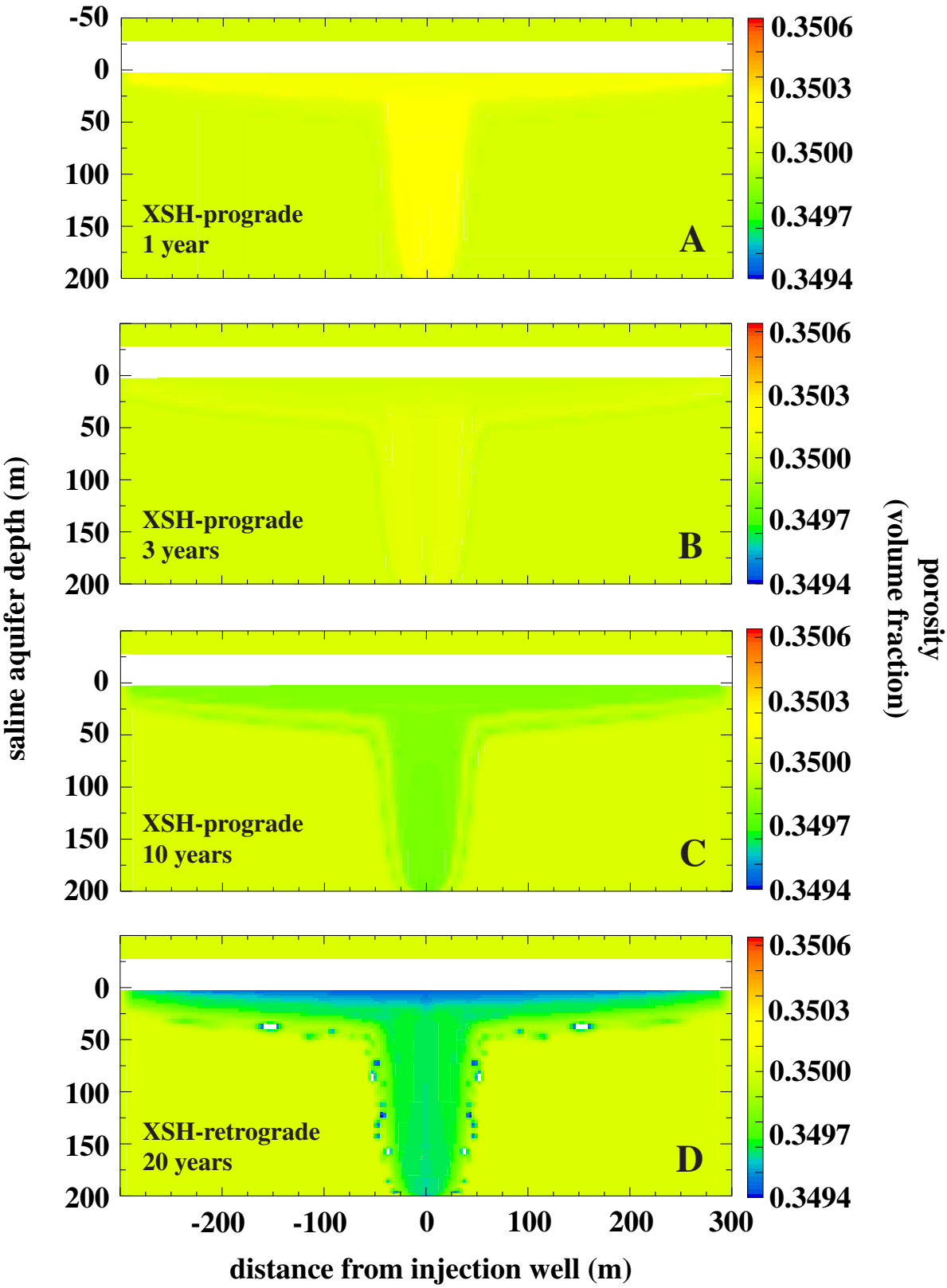

Figure 22: Evolution of porosity in the saline aquifer of model XSH during prograde (1, 3, and 10 years) and retrograde (20 years) sequestration.

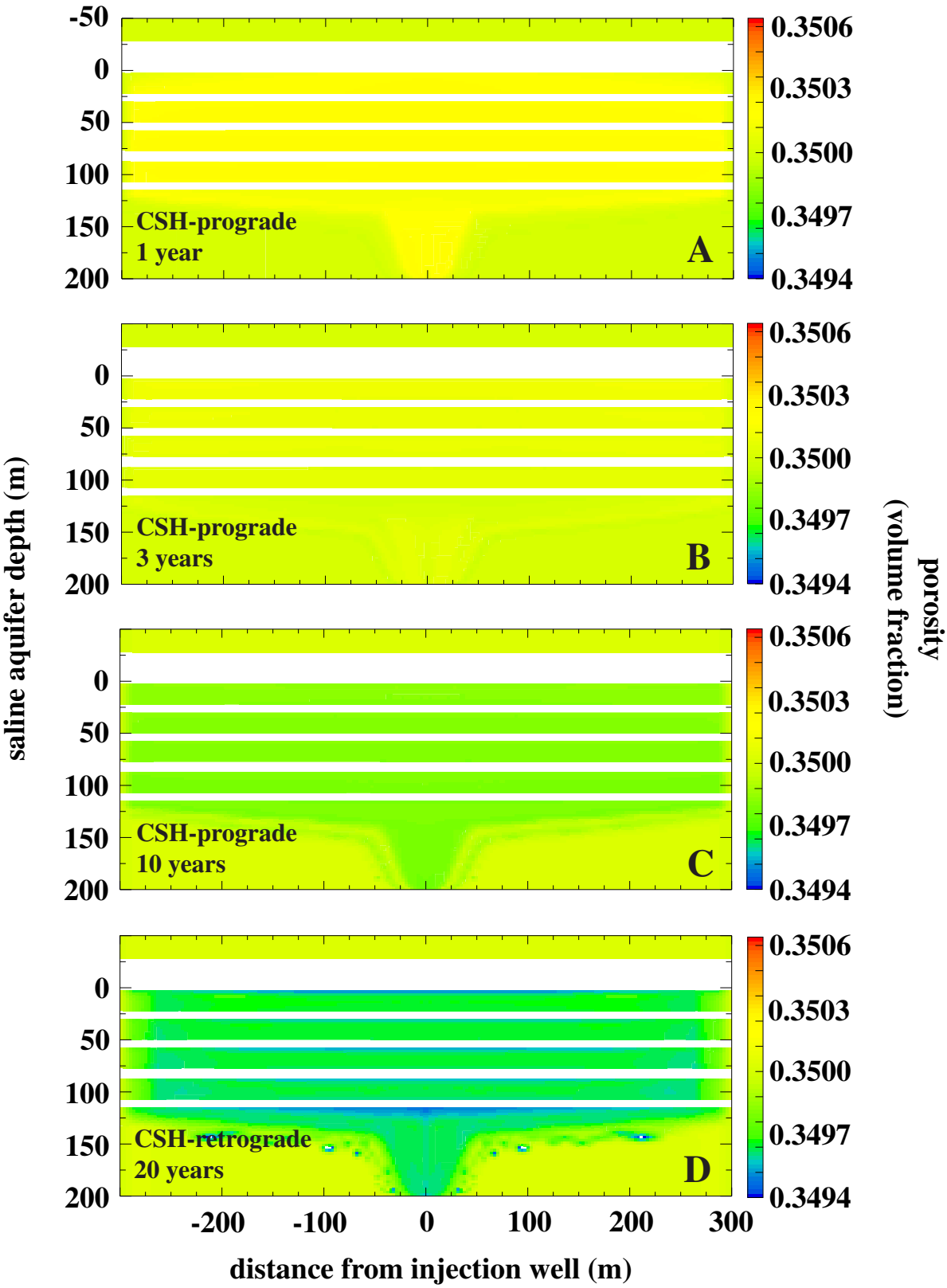

Figure 23: Evolution of porosity in the saline aquifer of model CSH during prograde (1, 3, and 10 years) and retrograde (20 years) sequestration.

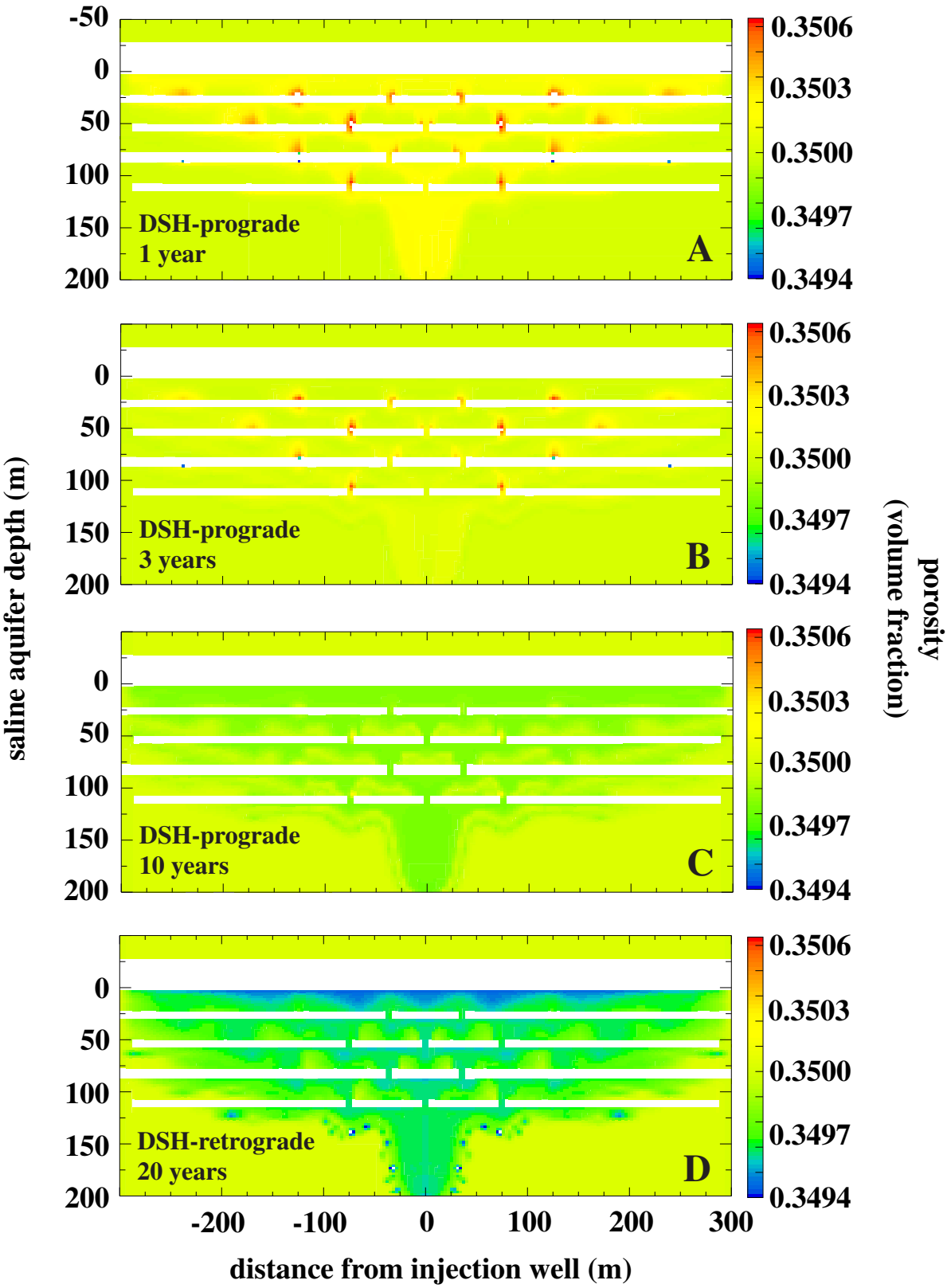

Figure 24: Evolution of porosity in the saline aquifer of model DSH during prograde (1, 3, and 10 years) and retrograde (20 years) sequestration.

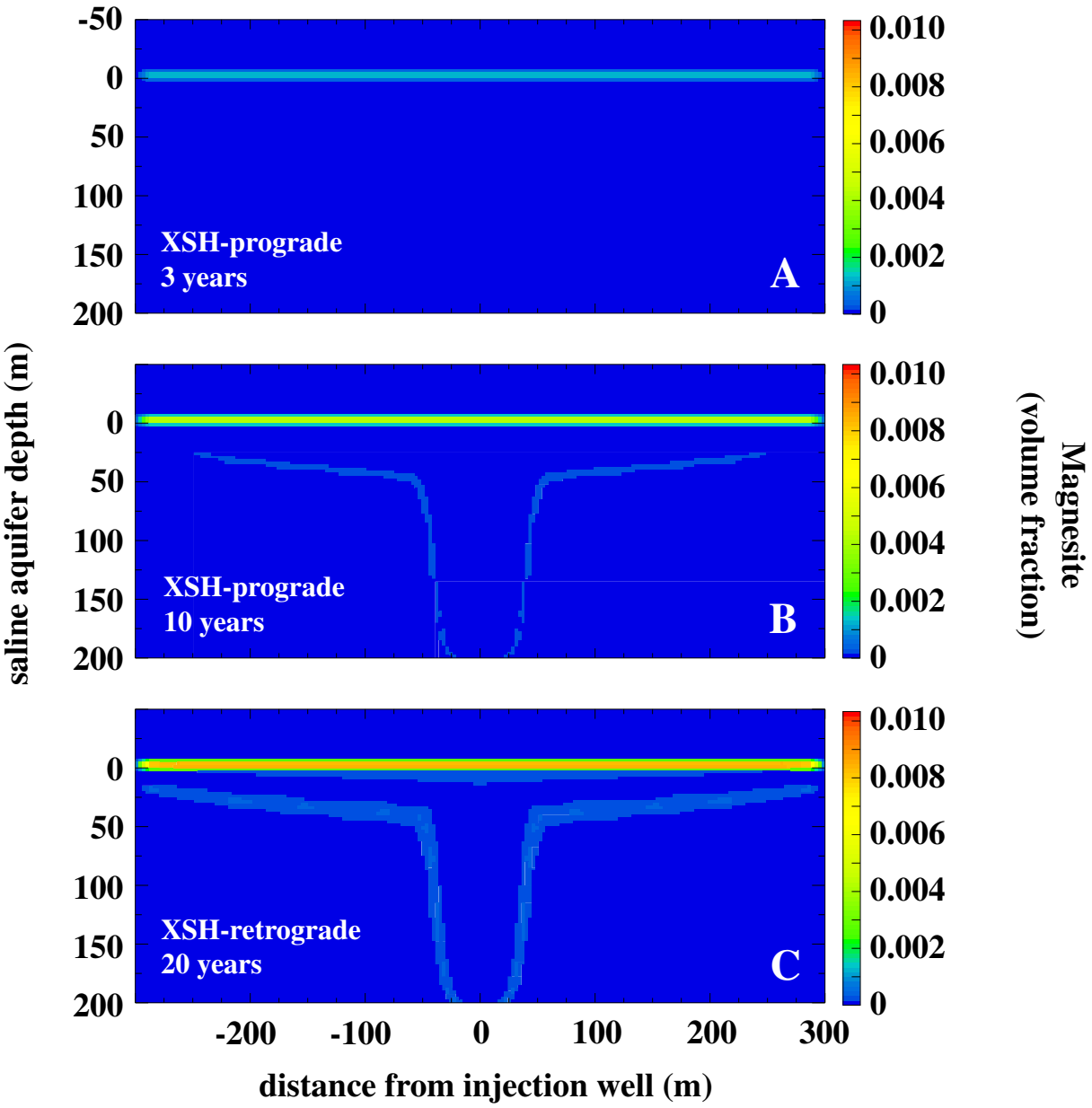

Figure 25: Evolution of Magnesite [$MgCO_3$] precipitation within the shale cap rock of model XSH during prograde (3 and 10 years) and retrograde (20 years) sequestration.

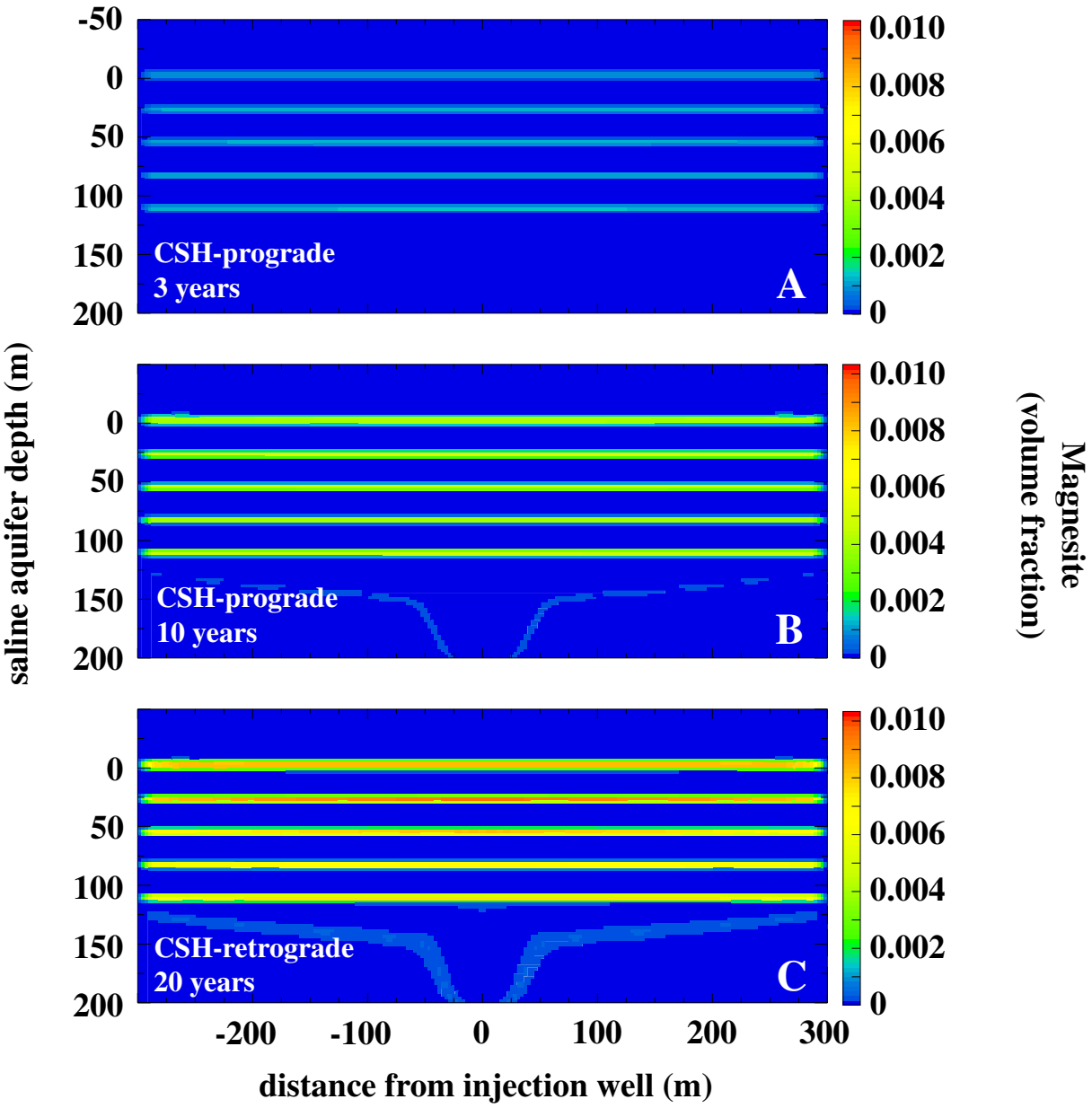

Figure 26: Evolution of Magnesite [$MgCO_3$] precipitation within the shale cap rock and intra-aquifer shales of model CSH during prograde (3 and 10 years) and retrograde (20 years) sequestration.

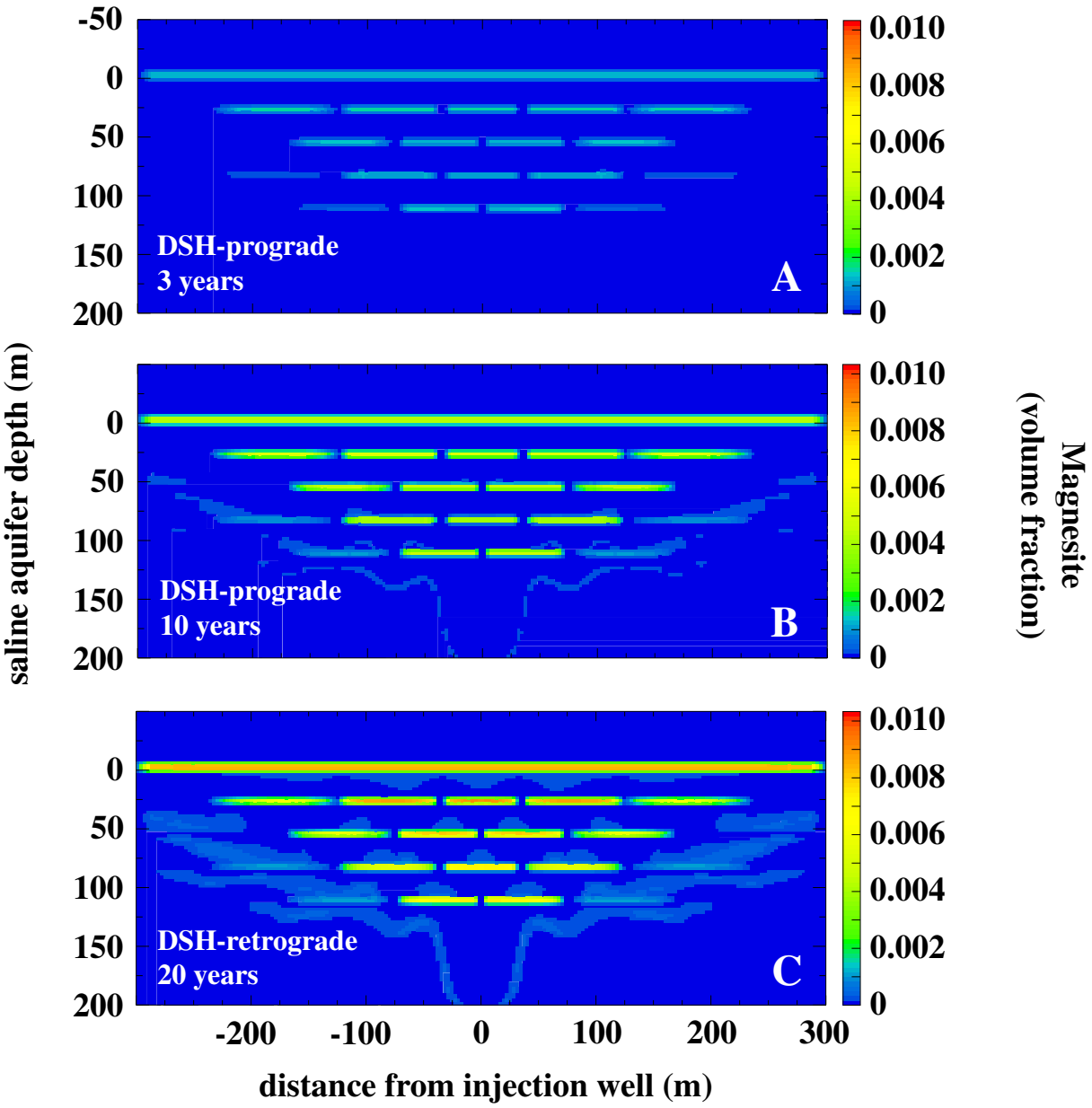

Figure 27: Evolution of Magnesite [$MgCO_3$] precipitation within the shale cap rock and intra-aquifer shales of model DSH during prograde (3 and 10 years) and retrograde (20 years) sequestration.

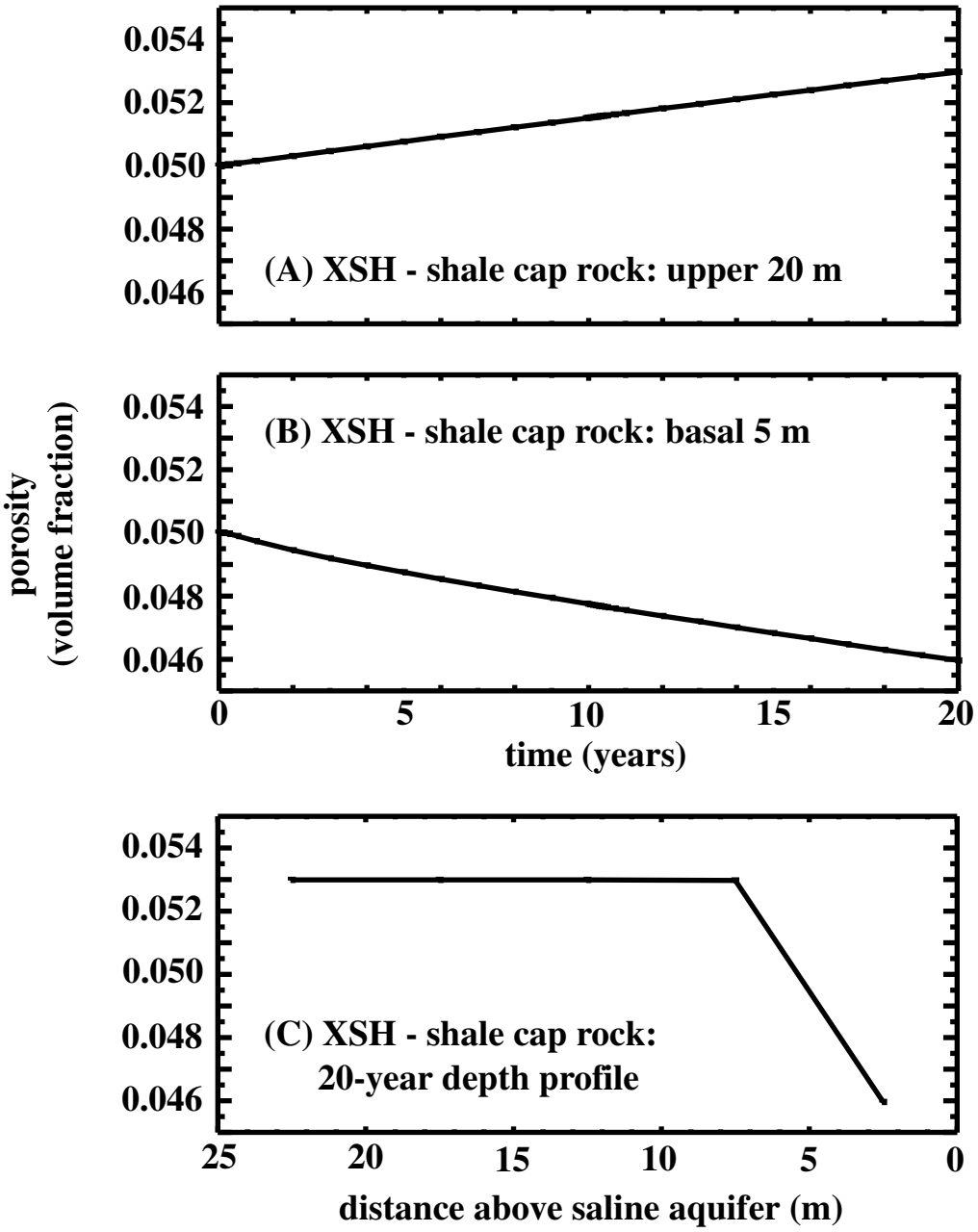

Figure 28: Porosity evolution and 20-year depth profile within the shale cap rock of model XSH. (A) porosity evolution within the upper 20 m [four layers of 5-m-thick grid cells], (B) porosity evolution within the basal 5 m [single 5-m-thick layer of grid cells that immediately overlies the saline aquifer], and (C) 20-year depth profile [data are plotted at grid-cell centers].

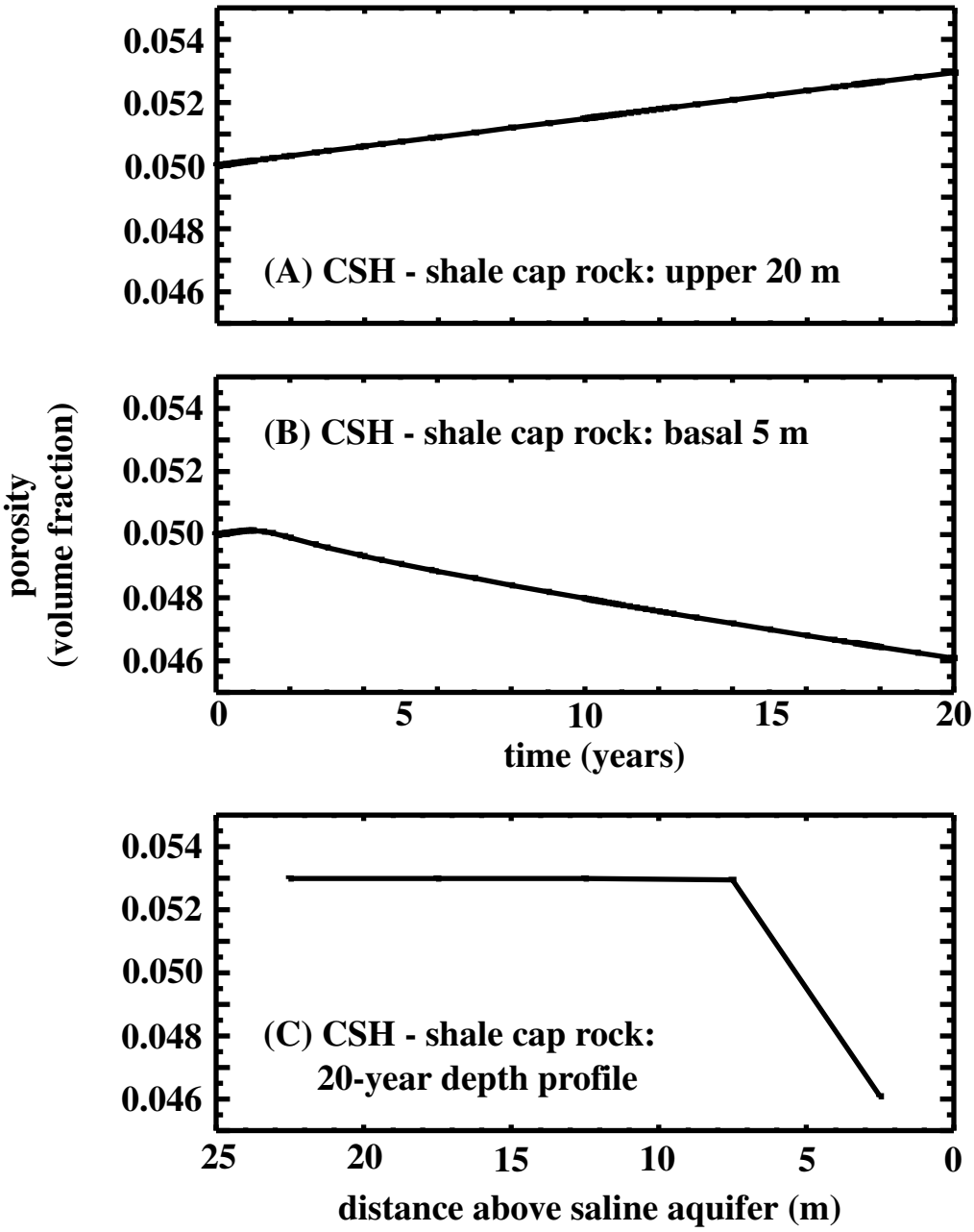

Figure 29: Porosity evolution and 20-year depth profile within the shale cap rock of model CSH. (A) porosity evolution within the upper 20 m [four layers of 5-m-thick grid cells], (B) porosity evolution within the basal 5 m [single 5-m-thick layer of grid cells that immediately overlies the saline aquifer], and (C) 20-year depth profile [data are plotted at grid-cell centers].

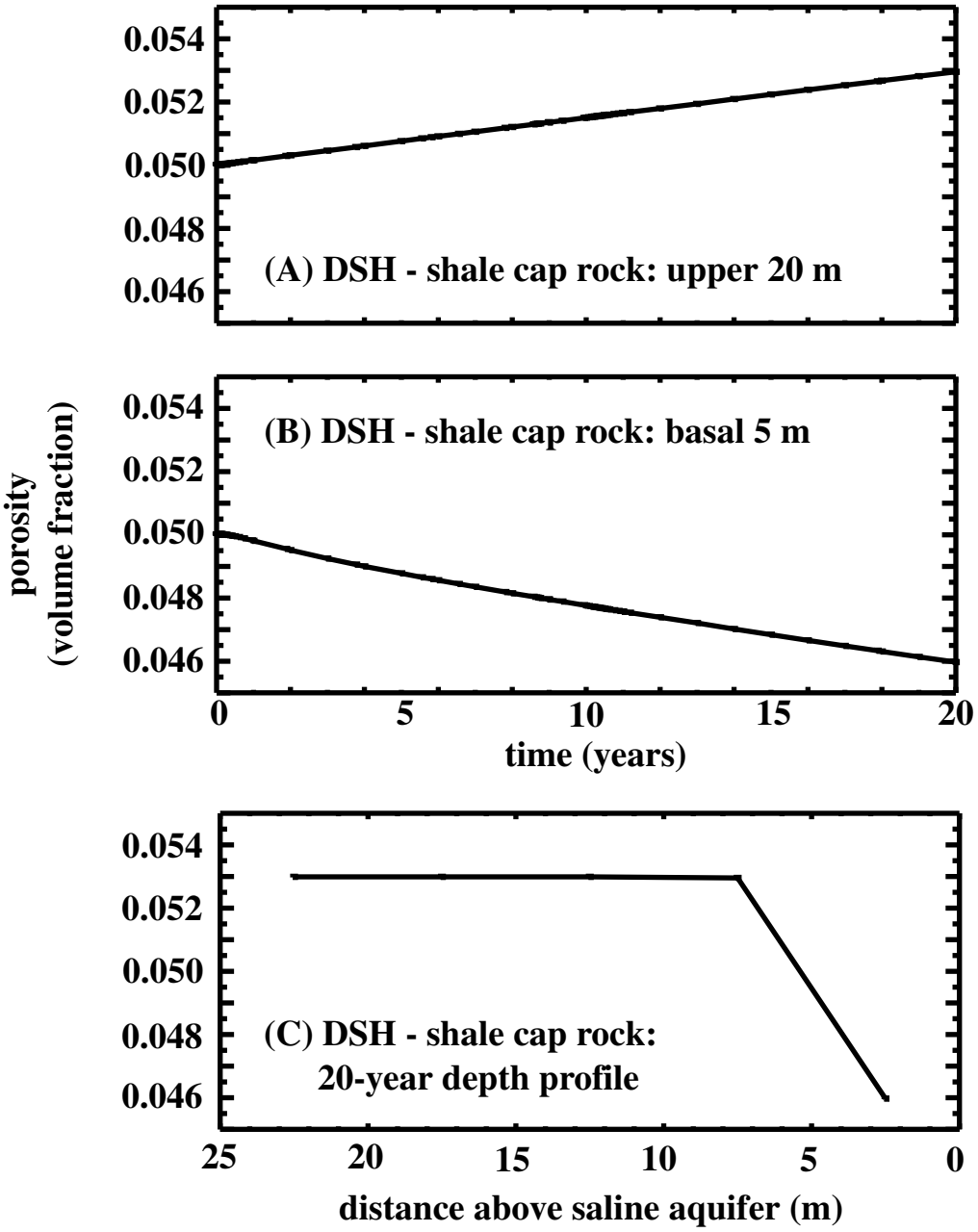

Figure 30: Porosity evolution and 20-year depth profile within the shale cap rock of model DSH. (A) porosity evolution within the upper 20 m [four layers of 5-m-thick grid cells], (B) porosity evolution within the basal 5 m [single 5-m-thick layer of grid cells that immediately overlies the saline aquifer], and (C) 20-year depth profile [data are plotted at grid-cell centers].